Journal Pre-proof

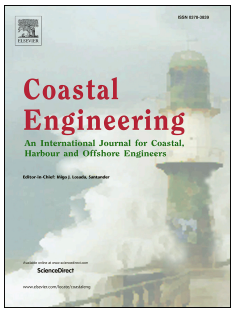

Wave overtopping flow striking a human body on the crest of an impermeable sloped seawall. Part II: Numerical modelling

Hao Chen, Jing Yuan, Deping Cao, Philip Liu

PII: S0378-3839(21)00052-1

DOI: https://doi.org/10.1016/j.coastaleng.2021.103892

Reference: CENG 103892

To appear in: *Coastal Engineering*

Received Date: 5 September 2020

Revised Date: 15 March 2021

Accepted Date: 23 March 2021

Please cite this article as: Chen, H., Yuan, J., Cao, D., Liu, P., Wave overtopping flow striking a human body on the crest of an impermeable sloped seawall. Part II: Numerical modelling, *Coastal Engineering*, https://doi.org/10.1016/j.coastaleng.2021.103892.

Author credit statement

1. Hao Chen: Designed and performed the numerical work, Prepared the original draft.
2. Jing Yuan: Reviewed and edited the draft, Administrated and supervised the project.
3. Deping Cao: Participated in research discussions, contributed to the draft of literature review.
4. Philip Li-fan Liu: Reviewed and edited the draft

Wave overtopping flow striking a human body on the crest of an impermeable sloped seawall. Part II: Numerical modelling

Hao Chen[a,b], Jing Yuan[a,*], Deping Cao[a], Philip Liu[a]

[a] *Department of Civil and Environmental Engineering, National University of Singapore, 1 Engineering Dr. 2, Block E1A 07-03, 117576, Singapore*
[b] *School of Engineering, University of Glasgow, Glasgow, UK*

Abstract

The present paper is the second of two companion papers on the investigations of wave overtopping flow striking a cylinder, which is the schematisation of a human body, on the crest of an impermeable sloped seawall with a deep foreshore. This paper numerically examines the detailed characteristics of the overtopping flow and the force on the cylinder in-line with the flow direction by using a volume-of-fluid (VOF) based Reynolds-Averaged Navier-Stokes (RANS) model. The numerical model is successfully validated against the experimental data on the wave overtopping flow depth and the inline force on the cylinder. The characteristics of the overtopping flow velocity are analysed using the validated numerical model. It is observed that the maximum depth-averaged flow velocity usually occurs before the maximum flow depth during an overtopping event, and decay of the overtopping velocity is much slower than the flow depth along the seawall crest. For plunging-breaker cases, the overtopping force on the cylinder usually comprises a cycle of a first impact peak, a main peak and a secondary peak. However, for surging-breaker cases, it is largely dominated by the main peak. The first impact peak is due to the impact of the tip of the overtopping flow on the cylinder, which usually has a higher flow velocity than the main stream. The main peak is generated by the asymmetric pressure distribution around the cylinder, which co-occurs with the maximum local momentum flux of the overtopping flow. As the force decreases after the main peak, there sometimes exists a secondary peak, which is formed by the complex free surface motion locally behind the cylinder. Additional numerical experiments are presented to demonstrate the applicability of a simple maximum force predictor developed in Part I. A prototype-scale simulation of irregular waves overtopping a sloped seawall is conducted to obtain the maximum force. The predictor also gives the maximum force in a wave-by-wave manner using the incident wave condition. These two approaches produce very similar estimates, suggesting that the predictor can be used for engineering applications.

Keywords: Wave overtopping; Fluid-structure interaction; Impact force; Wave breaking.

*Corresponding author, e-mail address: nusyuan@gmail.com

1. Introduction

Wave overtopping is one of the undesired hydraulic phenomena which may result in flooding at the coastal region. For sloped seawalls, wave overtopping occurs when waves break and run up on the seaward slope, reach the crest and pass over it. In designing a seawall, the key quantities describing wave overtopping are the mean overtopping discharge and the maximum overtopping volume, which must be limited below certain thresholds. These quantities can be obtained by either existing empirical formulas (EurOtop, 2018; Altomare et al., 2016; Van der Meer et al., 2009; Molines et al., 2019; Van der Meer and Bruce, 2013), or physical model tests (Pullen et al., 2009; Romano et al., 2015).

In many regions, the crest areas of seawalls are nice attractions for visitors, and public access to the seawall crest is often allowed. Unfortunately, in recent years, it has been reported in a number of publications that severe wave overtoppings have resulted in injuries or deaths of pedestrians on seawall crest. Allsop et al. (2003) stated that between 1999 - 2002, at least 12 people were dead in UK as being swept by wave overtopping. To gain insights of these tragedies, it is necessary to have a good understanding and modelling capability on how overtopping flow mobilises a pedestrian. Strictly speaking, neither the overtopping discharge rate nor the overtopping volume can directly explain how the overtopping flow endangers a pedestrian, though they have been used in some risk management guidelines for simplicity. Based on a variety of human stability experiments conducted in channel flume (Martínez-Gomariz et al., 2016; Russo et al., 2013; Jonkman and Penning-Rowsell, 2008), it is suggested that the flow parameters that define the flooding hazard posed to humans are the flow depth and velocity, which essentially determine the inline force on the human body. Therefore, these physical quantities are of particular interests in this paper, and they are the focus of the literature review below.

There are a number of publications discussing the overtopping flow depth and velocity by employing empirical formulas (Schüttrumpf and Oumeraci, 2005; Mares-Nasarre et al., 2019; Bosman et al., 2009; Van Bergeijk et al., 2019). These formulas are easy to use, and the empirical parameters in the formulas are calibrated based on the model-scale experimental data. However, each of these formulas has a clear range of applicability in terms of wave conditions, foreshore and slope of seawall. It is not always certain if these formulas are applicable for the conditions outside of their range of applicability. On the other hand, the experimental data on the velocity of overtopping flow is very limited. The main reason is the difficulty in obtaining reliable measurements, as the overtopping flow is generally very shallow, highly transient, and can be very aerated. Two companion papers (Ryu et al., 2007; Ryu and Chang, 2008) reported the laboratory measurements on wave overtopping on a rectangular structure. The particle image velocimetry (PIV) and bubble image velocimetry (BIV) were employed to measure the velocity, and the fiber optic reflectometer (FOR) was employed to measure the void fraction. In addition, dimensional analysis was performed and a formula was derived and calibrated for horizontal velocity along the deck. Similarly, in Chuang et al.

(2015, 2018), the highly aerated overtopping flow on a box-shaped structure was measured by the BIV. The overtopping flows were created by focused wave groups impinging on the front wall or directly on the deck. The velocities of the overtopping flow were successfully extracted and their relation to the impingement point was analysed.

In recent years, there have been a few publications on the investigations of overtopping flow striking onto structures near the coastal lines. Chen et al. (2015) developed an empirical formula for the overtopping loads on a vertical wall as a function of incoming wave conditions and seawall geometry. The formula was based on the concept of momentum flux, and several coefficients were introduced and calibrated based on scaled wave-flume experiments with a sloped (1:3 and 1:6) seawall. Further investigations were performed in Chen et al. (2016) for the maximum impact force on a wall induced by irregular-wave overtopping over a sloped seawall with a shallow foreshore. Van Doorslaer et al. (2017) developed design formulas for non-breaking wave overtopping and impacts on a storm wall. Three different approaches were suggested to calculate the impact forces on the wall, and their advantages and disadvantages were discussed. Large-scale laboratory tests have been performed by De Rouck et al. (2012) for breaking wave overtopping and impact on a storm wall. A so-called church-roof profile was reported for the recorded pressure and force on the wall, which shows a double-peaked shape for one impact event. Besides wind-generated waves, the impact force due to tsunami bore was also investigated in several research publications (Shafiei et al., 2016; Kihara et al., 2015). The bore was mostly generated by dam-break wave in these laboratory tests, and several phases during the impact process were identified and their characteristics were analysed. Yeh (2006) computed the drag force on a cylinder in the tsunami runup zone, where the flow velocity was extracted based on the solution of shallow water equation, and a drag coefficient was needed for computation of the drag force.

Numerical methods have been under fast development in the past decades and a variety of numerical models have been proposed to model wave overtopping process. The model performance depends on the solved equations and numerical technique, and relies heavily on a thorough calibration and validation process (Losada et al., 2008). Nonlinear shallow water equation (NSWE) has been widely used to predict wave overtopping in e.g., Hu et al. (2000); Stansby and Feng (2004). The computational cost for such models is rather low, which makes them suitable for long-term modelling and statistical analysis. However, NSWE is derived based on the assumption of hydrostatic pressure distribution. Therefore, it has restrictions on modelling of wave breaking process, and the offshore boundary condition has to be located close to the seawall in order to satisfy the shallow water limit.

Alternatively, the Navier-Stokes solvers are becoming popular within the coastal engineering community due to the rapid growth of computational resources. This kind of solvers can directly simulate breaking waves and the complex interaction process between overtopping flow and structures without substantial approximations. They are more expensive with regard to the computational time, but still affordable with the aid of supercomputing facilities. They have been widely adopted to simulate wave breaking and wave-

structure interaction process with varying success (Lin and Liu, 1998; Xie, 2013; Bradford, 2000; Bakhtyar et al., 2009; Wang et al., 2009; Chella et al., 2016; Ghadirian and Bredmose, 2020; Paulsen et al., 2014). Limited works have also been published on the modelling of wave overtopping flow using this solver, most of which are 2-dimensional cases (Losada et al., 2008; Hsiao and Lin, 2010; De Finis et al., 2020). There still lack benchmark cases on 3-dimensional overtopping flow interacting with structures. Actually, this is more complex than the simulations of pure wave breaking or wave-structure interaction problems, because overtopping flow is a post-breaking flow with small thickness and fast speed. Adequate resolution of the impingement of such flow onto the structures requires the solver to be sufficiently accurate and robust.

This paper is the second of two companion papers. In the first paper Cao et al. (2021) (hereafter referred to as Part I), we described the results from an experimental study, and derived an empirical predictor for quick estimation of the inline force due to overtopping flow. In the present paper, we shall numerically model the breaking wave induced overtopping flow interacting with a cylinder, which is the schematisation of a human body standing on the seawall crest. A volume of fluid (VOF) based Reynolds Averaged Navier-Stokes (RANS) solver is chosen in the present work. The primary goals of the paper are: (1) Thorough examination of the numerical model performance on dealing with simulating overtopping flow-cylinder interaction; (2) Detailed investigation of the overtopping flow characteristics and the physical process of the inline force on the cylinder; (3) Enlargement of the dataset for calibrating the empirical predictor proposed in Part I; (4) Confirming the applicability of the empirical predictor for practical applications.

The remainder of the paper is organised as follows. In Section 2, the governing equations, the setup and the convergence study of the numerical model are described. Then in Section 3, the model results are validated against the experimental data with regard to the wave propagation, breaking on seawall slope, the overtopping flow depth and the overtopping force on the cylinder. In Section 4, the characteristics of the overtopping flow velocity are investigated using the validated model, while detailed analysis of the overtopping force are provided in Section 5,. A case study at a prototype scale is presented in Section 6, which involves irregular incident waves. Finally, conclusions of this paper are given in Section 7.

2. Numerical model

2.1. Governing equations

A two-phase flow solver in the open source toolbox OpenFOAM is utilised as the numerical model, which models both the air and water phases. The governing equations for the solver are the continuity equation and the Reynolds Averaged Navier-Stokes (RANS) equations

$$\frac{\partial u_i}{\partial x_i} = 0, \tag{1}$$

$$\frac{\partial \rho u_i}{\partial t} + \frac{\partial \rho u_i u_j}{\partial x_j} = -\frac{\partial p}{\partial x_i} - g_j x_j \frac{\partial \rho}{\partial x_i} - \frac{\partial}{\partial x_j}\left(2\mu S_{ji} + \tau_{ji}\right), \tag{2}$$

where x_i is the Cartesian coordinate system where $i = (1, 2, 3)$, u_i is the Reynolds averaged velocity, g_i is the gravitation vector, ρ is the density, p is the pressure in excess and μ is the dynamic viscosity. The shear strain rate S_{ij} is defined as

$$S_{ij} = \frac{1}{2}\left(\frac{\partial u_i}{\partial x_j} + \frac{\partial u_j}{\partial x_i}\right), \tag{3}$$

and the Reynolds stress τ_{ij} is calculated according to the Boussinesq approximation

$$\tau_{ij} = -\rho\overline{u_i' u_j'} = 2\mu_T S_{ij} - \frac{2}{3}\rho k \delta_{ij}, \tag{4}$$

where the prime superscript denotes the turbulence fluctuations and the overbar signifies Reynolds-averaging process. k is the turbulent kinetic energy, δ_{ij} is the Kronecker delta, and μ_T is the eddy viscosity. A standard $k-\omega$ SST turbulence model is employed in the numerical model, which essentially models the turbulent kinetic energy k and the specific dissipation rate ω.

The free surface waves are generated by the waves2Foam toolbox developed by Jacobsen et al. (2012), which uses relaxation zones to generate incident gravity waves. The free surface is captured by using the concept of volume of fluid (Hirt and Nichols, 1981), where the water volume fraction field α is used to implicitly indicate the free surface position. The instantaneous local density and dynamic viscosity are specified in terms of the water volume fraction by the following constitutive equations

$$\begin{aligned} \rho &= \alpha\rho_w + \rho_a(1-\alpha); \\ \mu &= \alpha\mu_w + \mu_a(1-\alpha), \end{aligned} \tag{5}$$

where α is the water volume fraction and $\alpha \in [0, 1]$. Thus, the volume fraction of air is given by the complementary fraction $1-\alpha$. The subscript w and a refer to water and air, respectively. The isoAdvector approach proposed in Roenby et al. (2016) was adopted to advect the free surface, which is essentially an efficient two-step geometric VOF solver. In the first step, the free surface is explicitly reconstructed within each cell by applying the concept of isosurface. Secondly, from the reconstructed surface, the motion of the intersection lines between the cell face and the free surface is modelled to obtain their time evolution within a time step of the submerged face area. Readers are referred to Roenby et al. (2016) for details of the algorithm.

The numerical solution from RANS model provides field quantities, e.g., the water volume fraction, pressure and velocity distribution over the domain. Since the inline force on the cylinder is due to both the pressure and the surface shear stress in the present model, it is obtained by directly integrating the pressure and the surface shear stress over the instantaneous wet surface S_b as

$$F_i = \iint_{S_b} p n_i \, \mathrm{d}A + \iint_{S_b} (2\mu S_{ji} + \tau_{ji}) \cdot n_i \, \mathrm{d}A, \tag{6}$$

where F_i is the force component, n_i is the normal unit vector on the elementary surface $\mathrm{d}A$.

Table 1: Test conditions in the experiments in Part I. h is the still water depth, R_c is the freeboard, H is incident wave height, T is the wave period and I_r is the Iribarren number.

h [m]	R_c [m]	H [m]	T [s]	I_r [-]
$0.65 \sim 0.95$	$0.05 \sim 0.35$	$0.069 \sim 0.209$	$1.2 \sim 3$	$1.33 \sim 4.04$

It should be mentioned that although the isoAdvector method used in the numerical model is a geometric VOF method, it only reconstructs a temporary free surface within each time step. This free surface is not continuous and it is solely used for advecting free surface in the intermediate steps of the algorithm. It is not stored in the final solution, and the interface is finally represented implicitly by α. A native utility included in waves2Foam was used to extract the surface elevation η where

$$\eta = \int_{z_{\alpha=1}}^{z_{\alpha=0}} \alpha \, \mathrm{d}z + z_{\alpha=1}. \tag{7}$$

The integration of volume fraction was performed in a vertical line, and the free surface was located in-between the integration limits, i.e., $z_{\alpha=0}$ and $z_{\alpha=1}$. Actually, in Eq. (7), the position of free surface is averaged as the height of the water column above the level $z_{\alpha=1}$.

2.2. Model setup

In Part I, a set of experiments were conducted in a wave flume in the hydraulic laboratory at National University of Singapore. The wave flume is 36 m long, 1.3 m deep and 2 m wide. A piston-type wavemaker (HR Wallingford) was located at one end of the flume, and the seawall model with a 1:3 slope was constructed at the other end of the flume. The test conditions used in the experiments are presented in Table 1. Four capacitance type wave gauges CG1 - CG4 were installed to measure the surface elevations at a few selected locations in front of the seawall, and four ultrasonic probes US1 to US4 were used to measure the depth of the overtopping flow on the seawall crest. A cylinder was placed on the seawall crest, which was made of plastic pipe with an outer diameter of 6 cm. The upper end of the cylinder was mounted to a three-axis force sensor, which was bolted onto a rigid bar sitting on top of the flume. There was a tiny gap between the bottom of the cylinder and the seawall surface so that the cylinder did not touch the seawall surface during the experiment.

The numerical model is set up to reproduce the experiments in Part I. The domain has a length of 7.5 m from the left inlet boundary to the toe of the seawall. The width and height of the domain are 0.6 m and 1.3 m, respectively. The seawall was modelled as a smooth and impermeable slope with a height of 1 m and length of 3 m. A circular cylinder was located at 9 cm from the edge of the seawall, which is exactly the same as in the experiments. A relaxation zone was arranged at the left side of the numerical wave tank, starting from the inlet boundary and ending at 1.5 m to the toe of the slope. Within this relaxation zone,

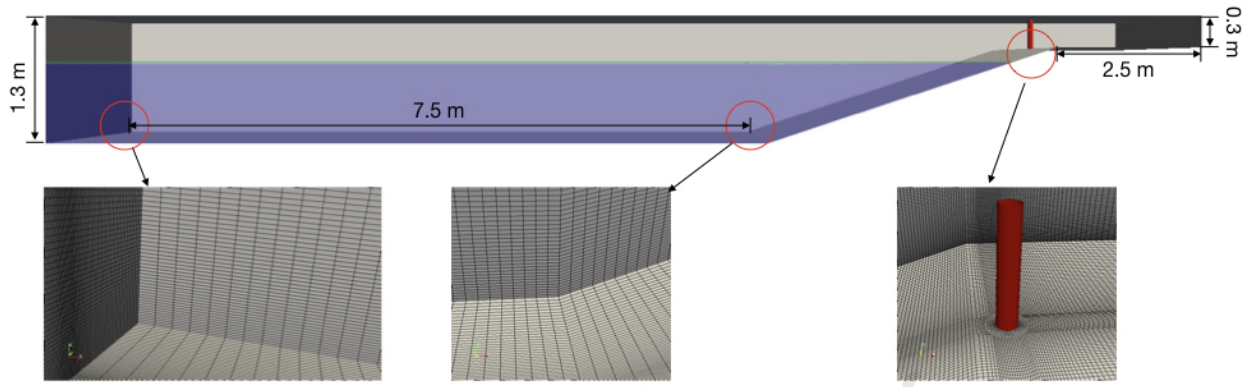

Figure 1: Overview of the numerical wave tank with zoom-in views of the block-structured mesh used in the numerical model. The purple area is the space initially occupied by the still water with a water depth of 0.85 m.

the waves were driven according to the stream function wave theory, and the velocity field u and the volume fraction field α were updated at each time step according to the relaxation function. At the right end of the numerical wave tank on the seawall crest, another short relaxation zone of 1 m was also applied to absorb the overtopping flow.

An example of the side view of the numerical wave tank is presented in Fig. 1 with zoom-in views of the mesh at some specific locations. A block-structured mesh with 18 blocks was generated using the native blockMesh toolbox, which is distributed within the OpenFOAM toolbox. Before waves arrive at the toe of the slope, the grid only needs to resolve wave propagation. Therefore, the grid in the wave-making zone is relatively coarse. On the slope, the waves start to shoal and eventually break, which produces the overtopping flow that further interacts with the cylinder. These hydrodynamic processes require a fine mesh to resolve. Hence, from the toe, the mesh is smoothly squeezed towards the cylinder. In the right relaxation zone, the grid is coarsened again as it is far away from the area that is of interest to us.

2.3. Convergence study

This section presents the convergence study for the above-introduced numerical model. The behavior of overtopping flow is determined by the type of wave breaking on the seawall slope, as indicated by many previous studies (e.g., Schüttrumpf and Oumeraci (2005)). For the tests presented in Part I of this study, two types of wave breaker, i.e., plunging breaker and surging breaker, were observed. With the same wave height and seawall slope, the surging-breaker tests have longer wave period than the plunging-breaker tests. It was also observed that the two types of breaker give quite different overtopping flows. Plunging-breaker induced overtopping flow can be highly aerated with a very high speed, while the surging-breaker induced overtopping flow is much 'greener' (less entrained air bubbles) and slower. Therefore, the convergence tests are performed for both cases. A representative case for surging breaker is chosen with $H = 0.20\,\mathrm{m}$,

Table 2: Mesh parameters for the convergence study. The cell size in the wave-making zone is the averaged size at the free surface area, as there is a smooth refinement from the far end near the wave-maker boundary to the area near the seawall. The cell size in the near-cylinder zone is the size of the first layer cell above the seawall's surface near the cylinder.

Grid NO.	Wave-Making Region		Near-Cylinder Region			Mesh NO. [million]
	Δx [mm]	Δz [mm]	Δx [mm]	Δy [mm]	Δz [mm]	
1	66	21	4.8	4.8	2.6	1.86
2	56	18	4.1	4.1	2.2	3.10
3	48	15	3.5	3.5	1.9	5.14

$R_c = 0.15\,\mathrm{m}$ and $T = 3\,\mathrm{s}$. For the plunging breaker, the wave period of the representative case becomes 2 s and the other two parameters remain the same.

Three different resolutions are selected for the convergence tests, and the details on the size of these three grids are given in Table 2. These three different grids are geometrically similar between each other, and the results from the test are presented in Fig. 2. Regarding the overtopping flow depth shown in Fig. 2(a), the time series for the surging-breaker case are quite smooth, and they agree with each other very well. For the plunging-breaker case, there are considerable high-frequency fluctuations. Such fluctuations are due to the entrained air phase, since the overtopping flow is highly aerated in this case. As described in Section 2.1, the elevation of free surface is obtained using Eq. (7), which represents an average height of the free surface over the vertical water column. Therefore, whenever the entrained air pass through the location of observation, there can be a sudden drop for the surface elevation, as shown in e.g., $t = 7.2\,\mathrm{s}$ for Grid 2. Despite of the high-frequency fluctuations, the general shape and the peak of the flow depth are about the same among the three predictions. Thus, the numerical results are convergent in terms of the overtopping flow depth.

Fig. 2(b) compares the overtopping inline force under different grid resolutions. Comparing to the prediction of surface elevation in Fig. 2(a), the effect of mesh size on the inline force seems to be more pronounced. For the plunging-breaker case, the three grids give very different initial peak when the flow just touches the cylinder (namely the first impact peak as introduced in Section 5.1). Following this, the magnitude of the peak occurring between 7.1 s and 7.3 s also seems to reduce from about 3.5 N for Grid 1 to 3.0 N for Grid 3. As mentioned above, the overtopping flow in this case is highly aerated. The flow's irregularity due to the entrained air phase produces significant fluctuations in the predicted inline force. This effect is most pronounced during the early stage of an overtopping event, since the front of the overtopping flow is more aerated than the tail. For the surging-breaker case, the agreement among the three predictions seems to be much better than that for the plunging-breaker case. This is mainly because the overtopping flow of the surging breaker is much less aerated.

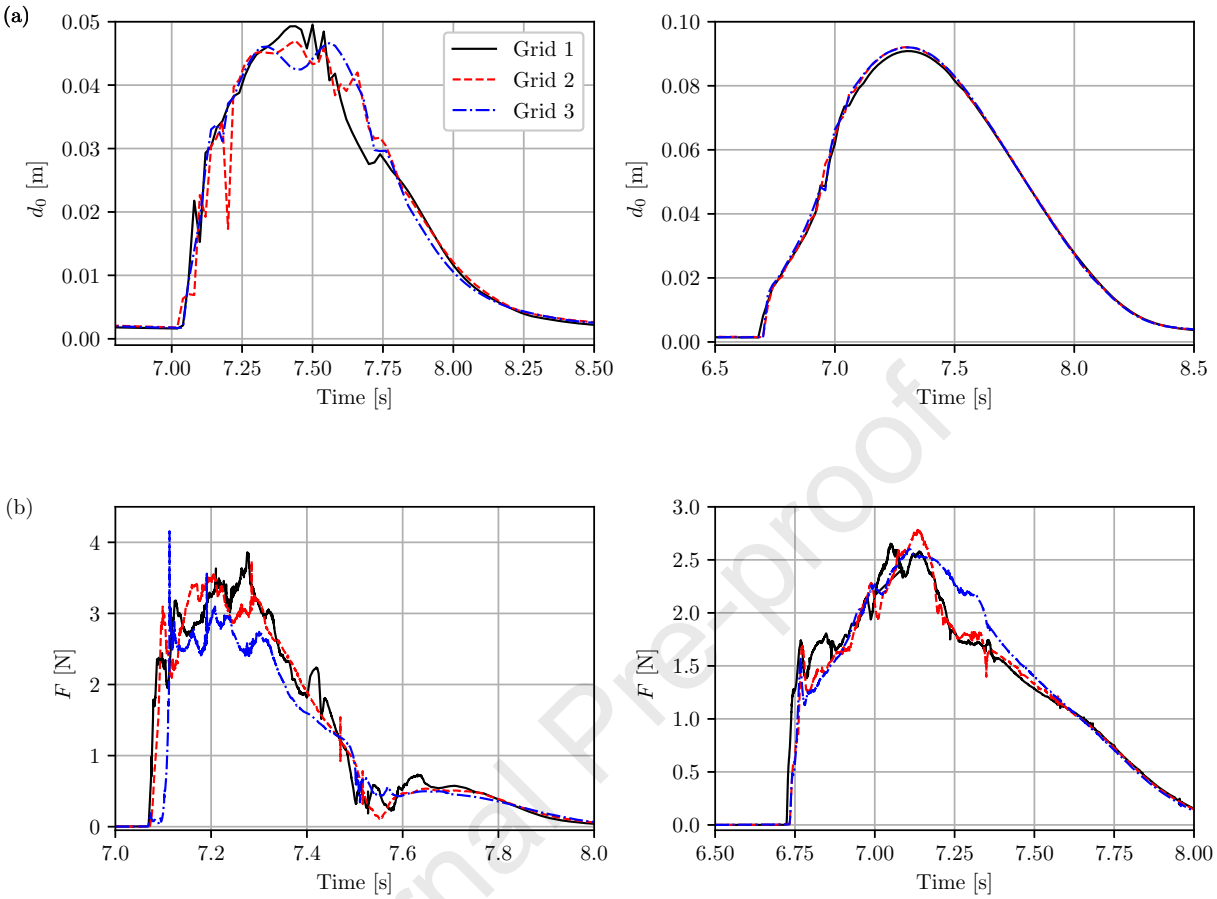

Figure 2: Results from the convergence test. (a) Computed depth of the overtopping flow at the edge of the seawall crest using different grid resolutions. (b) Computed inline force on the cylinder using different grid resolutions. Left column: plunging-breaker case ($H = 0.20\,\mathrm{m}$, $R_c = 0.15\,\mathrm{m}$ and $T = 2\,\mathrm{s}$). Right column: surging-breaker case ($H = 0.20\,\mathrm{m}$, $R_c = 0.15\,\mathrm{m}$ and $T = 3\,\mathrm{s}$).

Considering the comparison of the numerical results using three different resolutions as shown above, we conclude that the solution is convergent for the surging-breaker induced overtopping flow depth and inline forces. For the plunging-breaker case, the high frequency due to entrained air cannot be fully captured by the model, and a finer resolution does not necessarily give better prediction of the entrained air phase. In terms of the overall temporal variation of the flow depth and inline force, they are highly similar using the three grid resolutions. The discrepancy for the peak occurring between 7.1 s and 7.3 s, which is the target parameter of interest to us, is around 10%, which is small enough for our application. Thus, we consider that Grid 2 is fine enough to give a reasonable prediction of both overtopping flow and inline force, and it is applied in the following simulations.

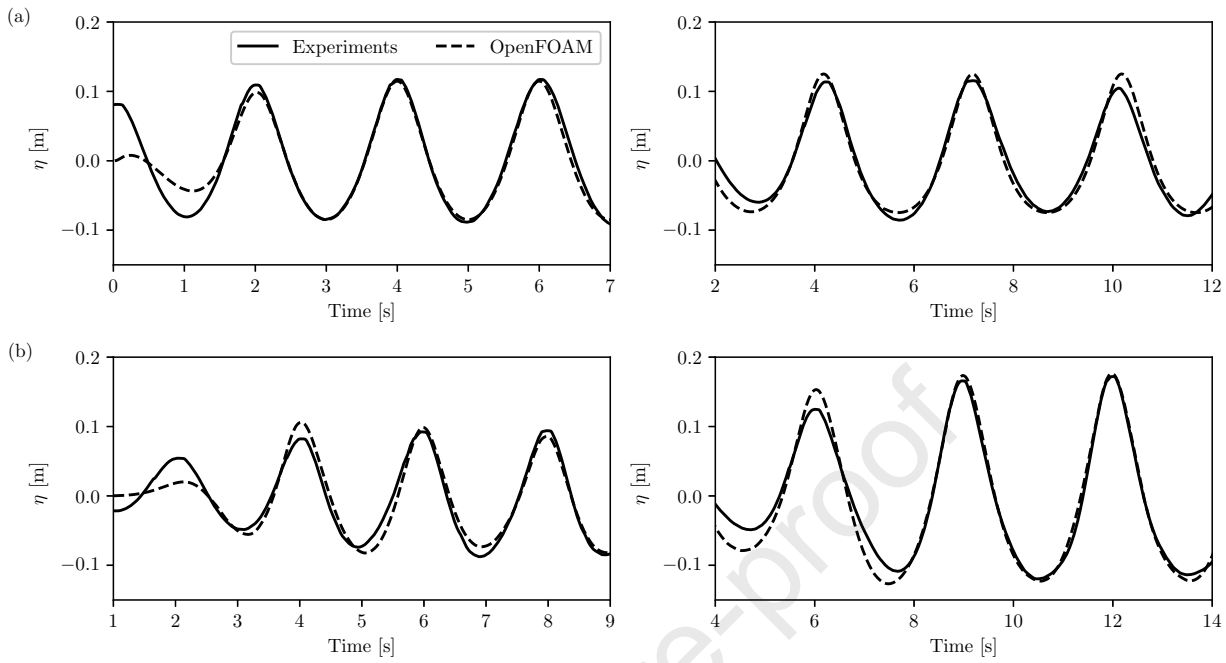

Figure 3: Comparison of the time series of the free surface elevation at (a) 2.5 m from the wave-maker; (b) the toe of the sloped seawall for the two representative cases. Left column: plunging-breaker case ($H = 0.20$ m, $R_c = 0.15$ m and $T = 2$ s). Right column: surging-breaker case ($H = 0.20$ m, $R_c = 0.15$ m and $T = 3$ s).

3. Model validations

In this section, the numerical model is validated against the experimental results obtained in Part I, including the free surface elevation near the wave-maker and at the toe of the sloped seawall, observed wave breaking processes on the slope of the seawall, the overtopping flow depth on the seawall crest and the inline force on the cylinder.

Comparison of the time series of the free surface elevation at 2.5 m from the wave-maker and at the toe of the sloped seawall is presented in Fig. 3 for both the plunging and surging breaker cases. Only the first wave cycle (e.g., $t = 1$ to 3 s in the left column) has a big discrepancy. This is because the initial movement of the piston-type wave-maker in the tests was not simulated by the relaxation zone in the numerical model. The model inaccuracy is generally $\mathcal{O}(1\,\text{mm})$ in both cases. The good agreement at $x = 2.5$ m (Fig. 3(a)) shows that the wave generation in the experiments were well simulated. The good agreement at the toe of the structure (Fig. 3(b)) is perhaps more important, because this requires that the reflected waves are well simulated, and a good simulation of wave reflection indicates wave breaking and associated energy dissipation on the seawall slope were successfully captured by our model.

The model performance on the wave breaking process is examined for the plunging-breaker case, as it involves much more complex process than the surging-breaker case, e.g., strong free surface deformation

and impingement of plunging jet on the slope of the seawall. The snapshots of wave breaking process from the experiments in Part I and the numerical model are given in Fig. 4. In Fig. 4(a), the free surface starts to overturn and leads to the formation of a plunging jet, as shown in Fig. 4(b). At the beginning of the impingement, the tip of the plunging jet touches the seawall slope, and a big air pocket is trapped inside the flow (Fig. 4(c)). The impingement turns the plunging jet into a violent water splash, and the trapped air pocket collapses and evolves into a breaking roller (Fig. 4(d)). Subsequently in Fig. 4(e), the water splash is organized into a runup jet along the seawall surface, which is highly aerated and has a very high speed. By comparing with the observations, the numerical model is capable to describe the overall process of the plunging-wave breaking, including the formation of the plunging jet flow, the impinging process and the subsequent roller. However, the highly aerated overtopping flow cannot be captured by the numerical model. In the experiments, air bubbles are distributed throughout the runup jet, so the flow appears 'white'. However, this is not fully reflected in the numerical results.

Direct comparison of the time series of the overtopping flow depth at a variety of streamwise locations (from the edge of the seawall, $x = 0$, to 0.44 m from the leading edge, $x = 0.44$ m) on the seawall crest is presented in Fig. 5. Note that in the numerical model, the overtopping flow depth is obtained based on Eq. (7), and in the experiments, it was measured using the ultrasonic probes. Synchronisation of the numerical and experimental results are based on the matching of the arrival time of the flow at the edge of the seawall for the first overtopping event. For the surging-breaker case (right column of Fig. 5), the time series of the overtopping flow depth is relatively smooth. The numerical model can well reproduce the peak of the flow depth, as the overall difference is within 10%. For the plunging-breaker case, both results have some oscillations due to entrained air as shown above, but the maximum overtopping flow depth is still captured by the model. We also want to highlight that the simulations and the measurements are well synchronised from $x = 0$ m to $x = 0.44$ m in both cases. This is a piece of evidence showing that the overtopping flow velocity is accurately predicted, otherwise a big phase separation would be obtained at $x = 0.44$ m (bottom row of Fig. 5) since we force the two signals to be well synchronised at $x = 0$ m. Unfortunately, we did not have direct flow velocity measurement for benchmarking.

Comparison between the predicted and measured inline forces on the cylinder is presented in Fig. 6. For the surging-breaker case, a single-peak temporal variation with moderate cycle-to-cycle difference is seen from the experimental results. The temporal variation of the force is captured well by the model, but an underestimation of the peak of the force is found, which is about $15\% \sim 20\%$. On the other side, regarding the validation of the inline force on the plunging-breaker case, considerable oscillations are also observed, which is similar to the flow depth. Regarding the main peak of the force, it is found that the underestimation still exists, but is less significant than that for a surging breaker. The average difference is reduced to around 10%.

The other 3D numerical simulations only reported data on inline force, due to the constrain of storage

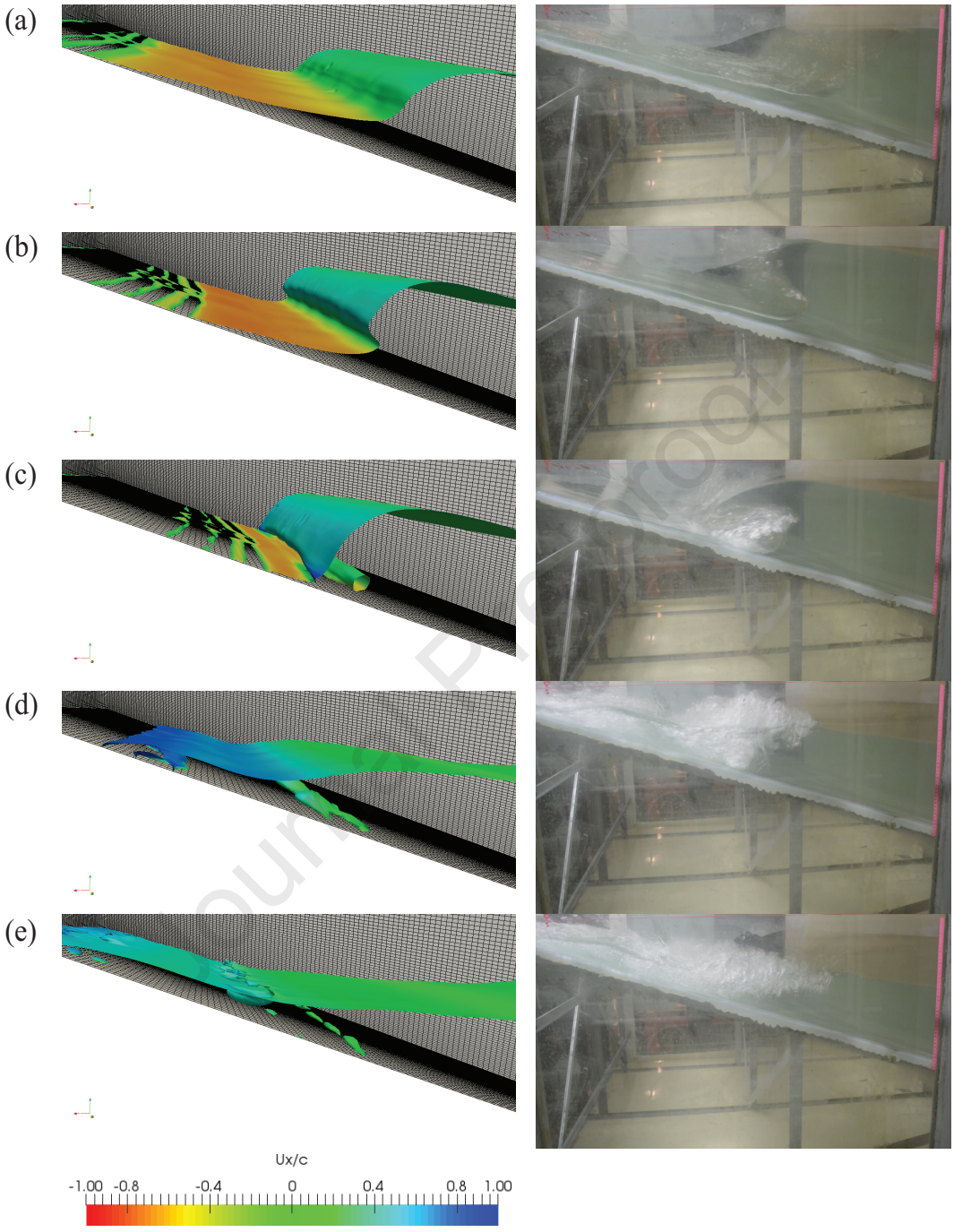

Figure 4: Snapshots of the plunging wave breaking process from the numerical simulations (left column) and the experiments (right column) at: (a) the time when the wave starts to overturn ($t_1 = 0$ s, $t_2 = 0$ s); (b) the time during the wave overturn ($t_1 = 0.14$ s, $t_2 = 0.18$ s); (c) the time when the overturned wave impinges the sloped seawall ($t_1 = 0.22$ s, $t_2 = 0.30$ s); (d) the time when the flow is strongly areated just after the impinge ($t_1 = 0.36$ s, $t_2 = 0.46$ s); (e) the time when the areated flow is further advected towards the seawall's crest ($t_1 = 0.46$ s, $t_2 = 0.64$ s). Here t_1 and t_2 are the time extracted from the simulations and the experiments, respectively. The free surface of numerical simulations is coloured with the horizontal velocity scaled by the wave celerity c.

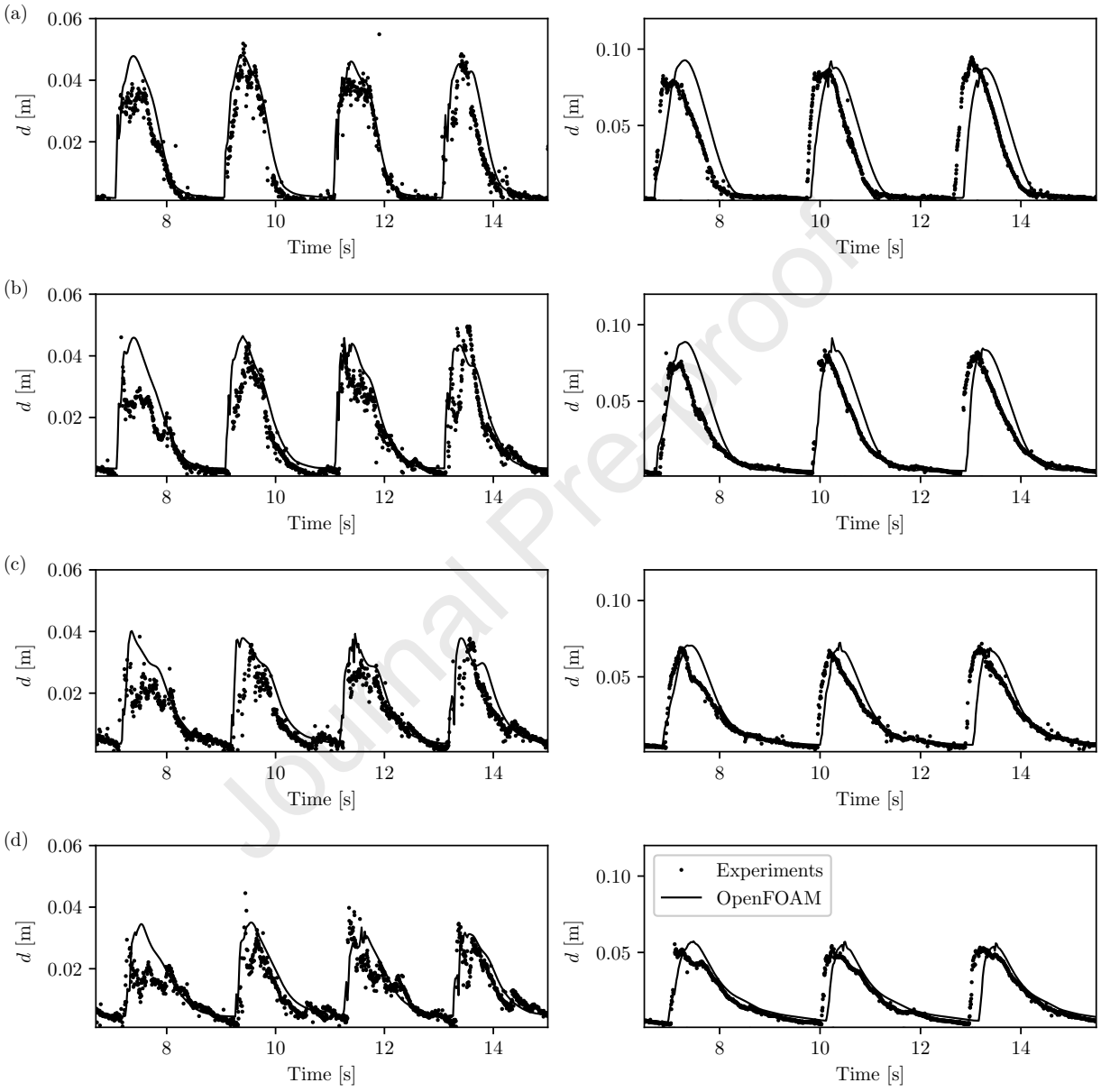

Figure 5: Comparison of the overtopping flow depth on the seawall crest at (a) edge of the seawall; (b) 0.06 m from the edge of the seawall; (c) 0.26 m from the edge of the seawall; (d) 0.44 m from the edge of the seawall. Left column: plunging-breaker case ($H = 0.20$ m, $R_c = 0.15$ m and $T = 2$ s). Right column: surging-breaker case ($H = 0.20$ m, $R_c = 0.15$ m and $T = 3$ s).

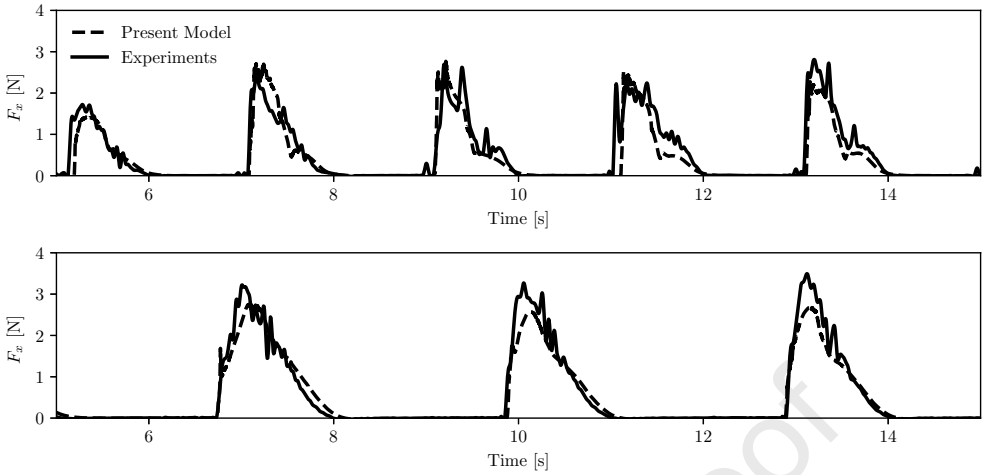

Figure 6: Comparison of the time series of the inline force on the cylinder due to plunging wave overtopping (upper) and surging wave overtopping (lower). The wave conditions are $H = 0.20\,\mathrm{m}$, $R_c = 0.15\,\mathrm{m}$ and $T = 2\,\mathrm{s}$ for the plunging-breaker case; $H = 0.20\,\mathrm{m}$, $R_c = 0.15\,\mathrm{m}$ and $T = 3\,\mathrm{s}$ for the surging-breaker case.

Table 3: Test conditions in the 2D numerical simulations. The slope is fixed as 1:3 for all the simulations.

h [m]	R_c [m]	H [m]	T [s]	I_r [-]	R_c/H [-]
$0.75 \sim 0.95$	$0.15 \sim 0.25$	$0.13 \sim 0.20$	$2 \sim 3$	$1.86 \sim 3.47$	$0.75 \sim 1.25$

space on the HPC. To get more data on overtopping flow depth and flow velocity, 15 additional 2-dimensional numerical simulations with the same domain size and similar mesh resolution in x and z directions are conducted, and the numerical results on overtopping flow depth are compared with the measured overtopping flow depth to enhance the validation of the numerical model. The test conditions for the simulations are presented in Table 3. Note that the test conditions between the simulations and the experiments do not exactly match. so here the comparison is based on the variation of the normalised flow depth.

The dimensional analysis in Part I suggests that the nondimensional maximum overtopping flow depth at the edge of the seawall d_{0m}/H is governed by three nondimensional parameters, namely the Iribarren number I_r, R_c/H where R_c is the freeboard and H is the wave height and $\cot\beta$ where β is the slope of the seawall. In the 2D simulations and experiments, the slope of the seawall is fixed as 1:3, so d_{0m}/H is only a function of I_r and R_c/H. Fig. 7 presents the comparison of d_{0m}/H between the numerical simulations and the experiments in a $I_r - R_c/H$ plane. The magnitude of d_{0m}/H is indicated by the colour. The two data clouds exhibit similar pattern of variations, i.e., the magnitude increases with I_r, but decreases with R_c/H, since surging breaker (high I_r) gives stronger overtopping flow than plunging breaker (low I_r), and a larger freeboard (or R_c/H) gives weaker overtopping flow. There is also a good matching of the symbol's colour, i.e., an experiential data point (full circle) has similar colour as the nearby simulation data point.

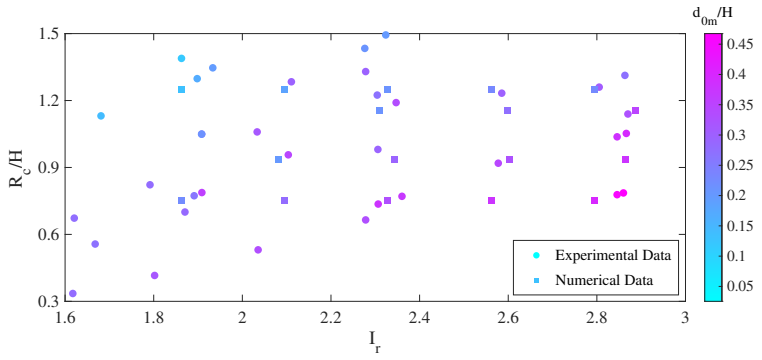

Figure 7: Comparison of the nondimensional maximum overtopping flow depth at the edge d_{0m}/H between the numerical and experimental results under a variety of wave conditions as shown in Table 3.

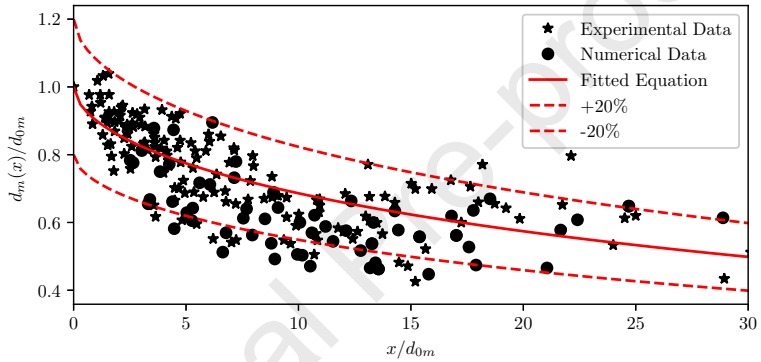

Figure 8: Validation of the numerical model on the decay of the maximum overtopping flow depth along the seawall crest. The fitted equation is given in Eq. (8), which is obtained based on the experimental data in Part I.

This suggests that the model can accurately predict the overtopping flow depth at the seawall's edge.

The numerical model is further validated against the experimental data on the decay of the maximum overtopping flow depth. The data is from the same set of 2D simulations, in which the overtopping flow depth is sampled at a distance of $x = 0\,\text{m}$, $0.2\,\text{m}$, $0.4\,\text{m}$, $0.6\,\text{m}$ and $0.8\,\text{m}$ from the edge of the seawall. Fig. 8 presents the nondimensional maximum overtopping flow depth $d_m(x)/d_{0m}$ at these locations with the experimental data. In addition, in Part I, an exponential equation (with about $\pm 20\%$ inaccuracy) was fitted based on the experimental data to describe the decay of the maximum overtopping flow, i.e.,

$$\frac{d_m(x)}{d_{0m}} = \exp\left[-0.104\left(\frac{x}{d_{0m}}\right)^{0.559}\right], \qquad 0 < x/d_{0m} < 45, \tag{8}$$

which is also presented in Fig. 8. It is observed that the numerical data (circles) cloud generally overlap with the experimental data cloud (stars) and is within the $\pm 20\%$ range of the fitted equation, but the majority of numerical data points are slightly below the line of the fitted equation with $5 < x/d_{0m} < 20$. This indicates that the numerical model tends to slightly underestimate the overtopping flow depth.

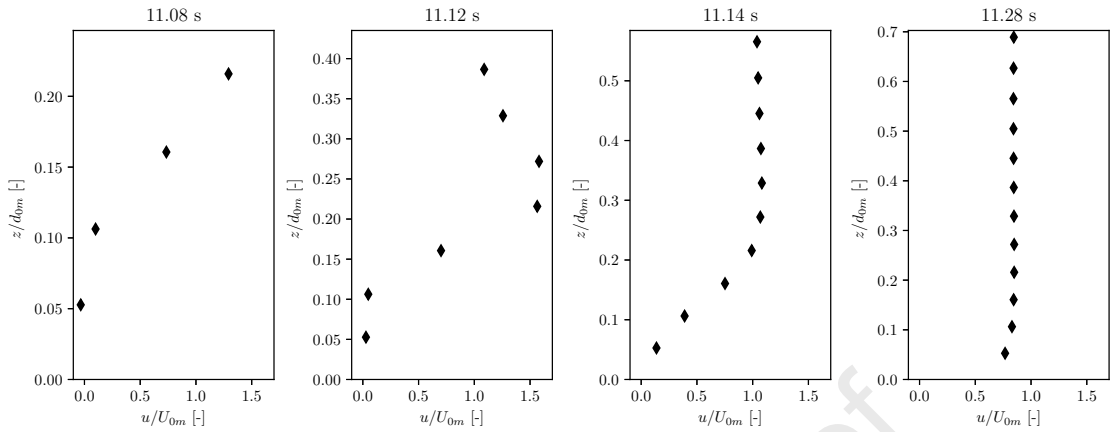

Figure 9: Evolution of the velocity profile for the overtopping flow for the plunging-breaker case at the edge of the seawall. d_{0m} and U_{0m} are the maximum flow depth and depth-averaged overtopping flow velocity at the edge of the seawall, respectively. The incident wave condition for this case is $H = 0.2\,\mathrm{m}$, $T = 2\,\mathrm{s}$ and $R_c = 0.15\,\mathrm{m}$.

The detailed validations in this section show that the numerical model can reasonably reproduce the lab tests in Part I, except that the maximum flow depth and the maximum overtopping force are slightly underestimated (by 10-20%). Thus it can be used to analyse the overtopping flow characteristics and the overtopping force on the cylinder.

4. Overtopping flow velocity

The overtopping flow velocity is an important quantity and it is directly related to the force on the cylinder, as introduced in Section 1. In this section, the numerical model is applied to investigate some key characteristics of the overtopping flow velocity, which cannot be directly measured in the tests of Part I. The numerical results are obtained from the same set of 2D simulations introduced in Section 3.

In Fig. 9, the evolution of the velocity profile at the seawall's edge is presented for the plunging-breaker case. As the numerical results are quite repeatable and cycle variation is negligible, it is not necessary to cycle-average the results. Instead, a representative overtopping event is selected, which corresponds to the third overtopping wave cycle in Fig. 5(a). The instantaneous velocity and flow depth are nondimensionalised by the maximum depth-averaged velocity and the maximum flow depth at $x = 0\,\mathrm{m}$ during this event. It is found that initially when the tip of the flow just arrives at the edge of the seawall, the flow is largely non-uniform across the depth. The top layer has a faster flow velocity than the bottom layer. The flow velocity near the bottom is rapidly accelerated and eventually the overtopping flow at the edge of the seawall becomes almost uniform vertically before the depth reaches the maximum. This means that a shallow-water approximation, which assumes a depth-uniform flow velocity, is applicable except for the very beginning of an overtopping cycle.

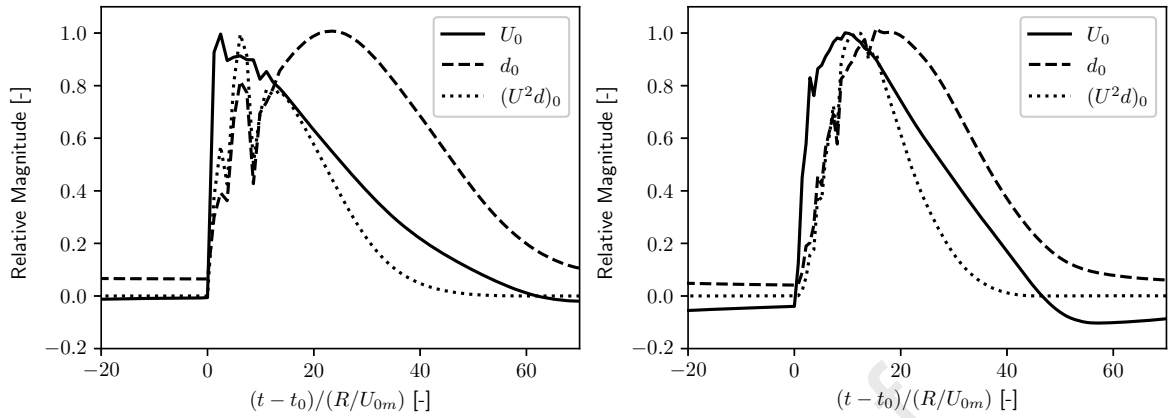

Figure 10: Time series of the overtopping flow depth d_0, the depth-averaged velocity U_0 and the momentum flux $(U^2d)_0$ at the edge of the seawall for one particular overtopping event. The relative magnitude is defined as the ratio between the instantaneous magnitude of the quantity and the maximum value during this cycle. t_0 is when the overtopping flow arrives the edge of the seawall. R is the radius of the cylinder. Left: plunging-breaker case ($H = 0.20\,\mathrm{m}$, $R_c = 0.15\,\mathrm{m}$ and $T = 2\,\mathrm{s}$). Right: surging-breaker case ($H = 0.20\,\mathrm{m}$, $R_c = 0.15\,\mathrm{m}$ and $T = 3\,\mathrm{s}$).

Fig. 10 presents time series of the overtopping flow depth d_0 and the depth-averaged velocity U_0 at the edge of the seawall for both the plunging and surging breaker cases. It is observed that there is a difference between the occurrence time of the maximum depth-averaged flow velocity and the maximum flow depth. For both cases, the flow velocity reaches its maximum before the flow depth develops to its maximum. We also present the time series of the momentum flux $(U^2d)_0$, which has been defined and used in (Hughes, 2004a,b). The maximum momentum flux, as can be expected, occurs between the maximum depth and maximum velocity. The difference of the occurrence time between the maximum flow velocity and the maximum flow depth is more pronounced for the plunging-breaker case rather than the surging-breaker case. This can be represented by the local Froude number defined as

$$F_r = \frac{U_{0m}}{\sqrt{g d_{0m}}}, \tag{9}$$

where d_{0m} and U_{0m} are the maximum overtopping flow depth and the depth-averaged flow velocity at the edge of the seawall. The Froude number for the plunging breaker case reaches 2.75, which indicates that it produces a very supercritical flow with fast speed and very thin layer. The Froude number for the surging breaker case drops to 1.25 as the flow is slower with thicker layer.

The Froude number of the overtopping flow at the edge of the seawall is presented in Fig. 11, given the wave conditions shown in Table 3. It is found that the Froude number has a strong dependence on the Iribarren number. As Iribarren number increases from 1.8 to 3.5, the Froude number decreases from 3.0 to 1.25. A linear fitting can well describe the relation between the Froude number of the overtopping flow Fr

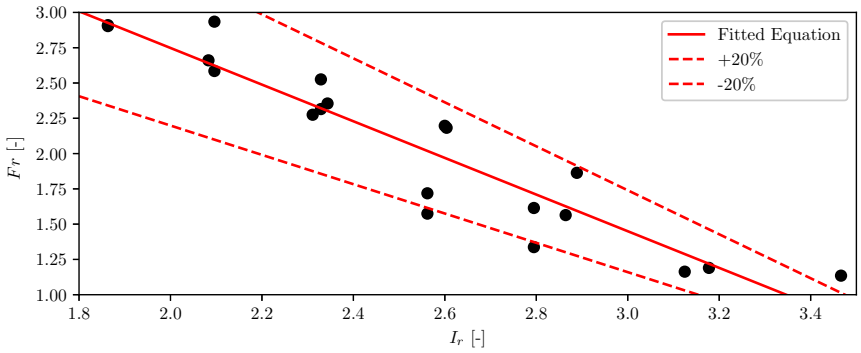

Figure 11: Variation of the Froude number of the overtopping flow at the edge of the seawall under different Iribarren number I_r. The fitted equation is Eq. (10).

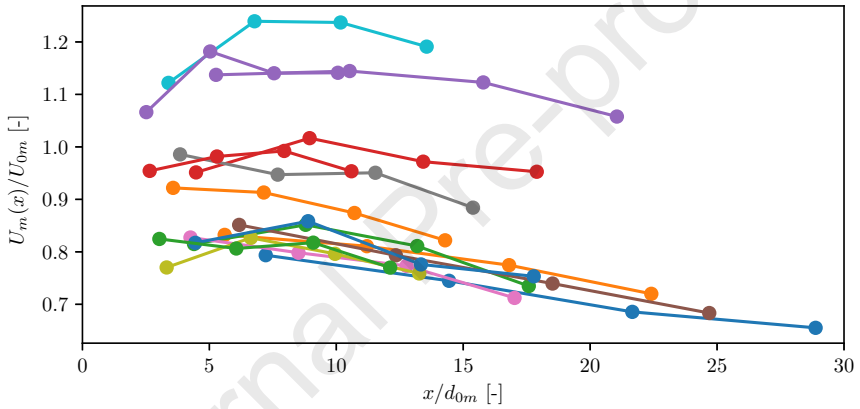

Figure 12: Decay of the maximum depth-averaged overtopping flow velocity along the seawall crest. Each line represents one simulation.

at the edge of the seawall and the Iribarren number with ±20% uncertainty, i.e.

$$Fr = -1.30I_r + 5.35, \qquad 1.8 < I_r < 3.5. \tag{10}$$

Decay of the maximum depth-averaged velocity along the seawall crest is presented in Fig. 12, where the decay of the velocity is sampled at $x = 0.2\,\mathrm{m}$, $x = 0.4\,\mathrm{m}$, $x = 0.6\,\mathrm{m}$ and $x = 0.8\,\mathrm{m}$. The four data points connected by each solid line are obtained from the same case at these four locations. In general, comparing with the exponential decay of the overtopping flow depth, the depth-averaged flow velocity is unlikely to decay significantly. Instead, a constant flow velocity can be maintained for a fairly long distance from the edge of the seawall, as most of the data points fall within the range of $0.7 < U_m(x)/U_{0m} < 1.2$ for $x/d_{0m} < 30$.

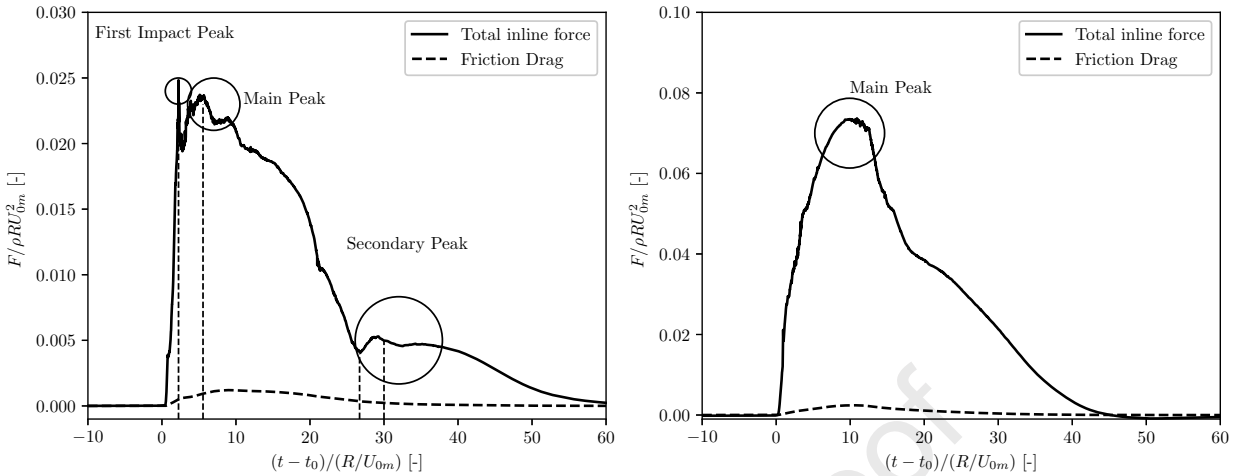

Figure 13: The total inline force and the friction drag during a typical overtopping event for both the plunging-breaker case (left) and surging-breaker case (right). For the plunging-breaker case, the first impact peak, the main peak and the secondary peak are identified, while for the surging-breaker case, only the main peak is identified. t_0 is when the overtopping flow encounters the cylinder. R is the radius of the cylinder. The four vertical dash lines in the left figure denote the time instants at $t' = 2.24$, $t' = 5.55$, $t' = 26.70$, $t' = 30.0$, respectively. Left: plunging-breaker case ($H = 0.20\,\mathrm{m}$, $R_c = 0.15\,\mathrm{m}$ and $T = 2\,\mathrm{s}$). Right: surging-breaker case ($H = 0.20\,\mathrm{m}$, $R_c = 0.15\,\mathrm{m}$ and $T = 3\,\mathrm{s}$).

5. Inline force on the cylinder

When overtopping flow encounters a cylinder, their interaction produces the force in-line with the flow direction on the cylinder. A typical inline force cycle is presented in Fig. 13 for both the plunging and surging breaker cases. For easy comparison, the time is normalised as $t' = (t - t_0)/(R/U_{0m})$, and the overtopping force is normalised as $F' = F/\rho R U_{0m}^2$. The friction drag force is presented together with the total inline force, and it can be easily seen that the contribution from friction drag is a few percentage of the total inline force, which can be neglected. The pressure induced form drag makes the most important contribution to the total inline force.

There can be multiple peaks for the inline force during one overtopping event, especially for the plunging-breaker case. To facilitate the discussions on the inline force, a few terms are defined first, namely the first impact, the main and the secondary peaks. For the plunging-breaker case, the first impact peak occurs when the tip of the overtopping flow touches the cylinder at $t' = 2.24$. The duration is extremely short and the force is rapidly reduced after it. The main peak occurs around $t' = 5.55$, and it is due to the interaction of the main stream of the overtopping flow with the cylinder. The duration of this one is considerably longer than the first impact peak, and there can exist local variations due to e.g., entrained air bubbles or surface ripples. During the decrease stage of the inline force, there exists an additional load cycle, starting with the dip at $t' = 26.7$ and reaches its maximum around $t' = 30$. We refer this phenomenon as the secondary load cycle and its associated peak is called the secondary peak. Usually the magnitude of the secondary peak

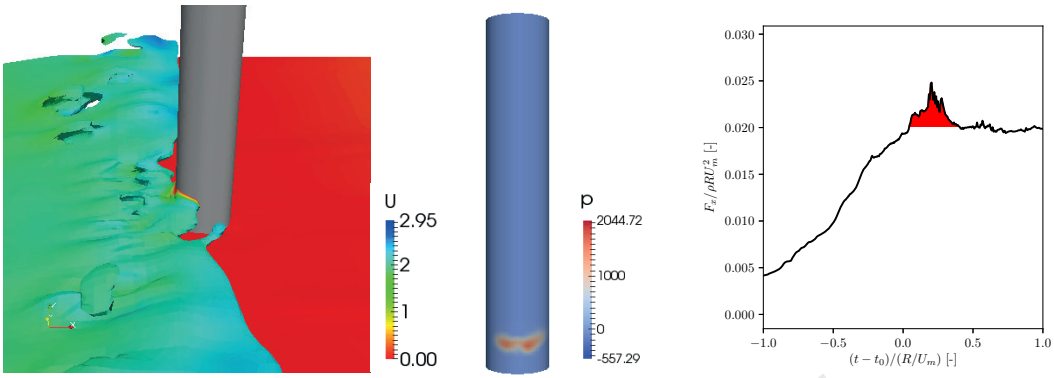

Figure 14: Illustration of the first impact peak. Left: A snapshot when the first impact peak occurs. Middle: Pressure field on the cylinder when the first impact peak occurs. Right: Inline force time series on the cylinder, where the effect of first impact peak is highlighted with red shaded area. t_0 is the time when impact occurs. ρ is water density.

is much smaller than the main peak. For most surging-breaker cases (including the representative case in the right panel of Fig. 13), only the main peak can be identified during one overtopping event, although occasionally the other two may also appear. More in-depth discussions on these features are as follows.

5.1. First impact peak

To illustrate the first impact peak, we extract a snapshot of the plunging-breaker case when the first impact peak occurs, and present it together with the time series of the inline force in Fig. 14. The first impact peak is induced when the tip of the overtopping flow just slams onto the cylinder. On the surface of the cylinder, a small area with a high pressure (over 2000 Pa) is created around the point of impact. The duration of the impact is extremely short, which is about $0.5(R/U_m)$, or in the order of 0.001 s to 0.01 s.

The first impact peak is more obvious for plunging-breaker cases, and it even may not occur for some surging-breaker cases. As introduced above, the plunging breaker produces a thin layer of overtopping flow with very fast speed. For example, the flow velocity in Fig. 14 is up to $2-3$ m/s, while the thickness of the flow is only a few millimetres at the tip. This naturally creates a condition for the first impact peak to occur. Furthermore, for the same case, the numerical model tends to predict a more obvious first impact peak than the laboratory tests, as shown in Section 3. One possibility is that in the experiments, there was a tiny gap between the cylinder's bottom and the surface of the seawall crest (a necessary configuration for measuring the inline force). Therefore, the tip of the overtopping flow may partially pass beneath the cylinder in the experiments, which leads to a reduced first impact peak. Furthermore, deformation and vibration of the cylinder may also reduce the first impact peak. We also find a strong cycle-to-cycle variation for the first impact peak. This is not surprising, as we have argued that the first impact peak is associated with the local behaviour of the overtopping flow at the tip region. In each overtopping cycle, the local shape and the curvature of the tip can be different, leading to different magnitudes of the first impact peak.

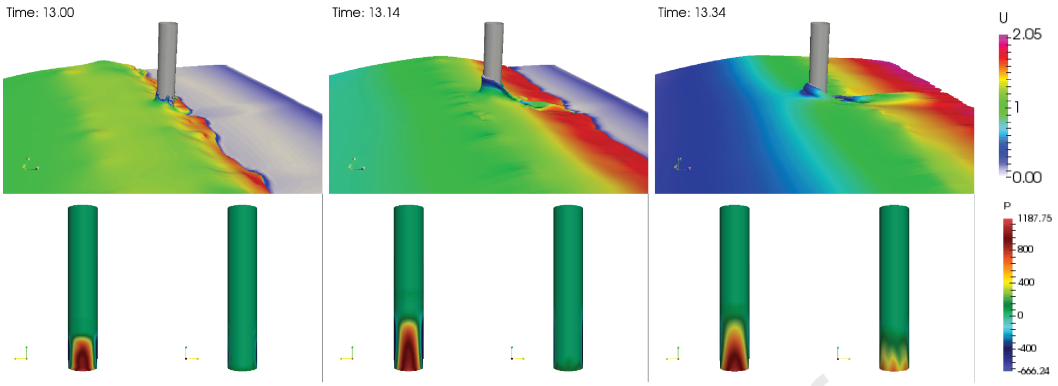

Figure 15: The snapshots of the flow (upper column) and the pressure distribution on the front and back side of the cylinder (lower column, left: front side, right: back side) before the main peak ($t = 13.00$ s), when the main peak occurs ($t = 13.14$ s), and after the main peak ($t = 13.34$ s). The results are from the surging-breaker case, and the incident wave condition is $H = 0.20$ m, $R_c = 0.15$ m and $T = 3$ s.

We shall emphasize that in the context of overtopping flow-human interaction, a correct estimate of the first impact peak on the circular cylinder is secondary, since it is strongly related to the local curvature of the body, which can not be well represented by a simple cylinder. Furthermore, human body is not completely rigid, i.e., the muscle and skin are considerable flexible. Essentially, the finite stiffness of human body makes the problem associate with hydroelasticity. This is out of the scope of the present paper and further investigations are needed.

5.2. Main Peak

The main peak is the consequence of the interaction between the cylinder and the main stream of the overtopping flow. Fig. 15 presents the snapshots for the surging-breaker case when the main peak occurs. When the main body of overtopping flow hits the cylinder, water is piled up in front of the cylinder due to its blockage. Furthermore, there is a tiny runup jet flow climbing upwards along the cylinder. As the flow wraps around the cylinder, the free surface level drops continuously, so there is much less water in the wake region. As can be expected, the asymmetry distribution of immersed area around the cylinder leads to an asymmetry distribution of pressure acting on the cylinder's surface, as shown in the lower row in Fig. 15. The main peak occurs when this asymmetry is maximised at around $t = 13.14$ s. To further demonstrate this, we perform vertical line integration of the total pressure on the cylinder's surface (from bottom to free surface), and present the distribution of this integrated pressure along the perimeter of the cylinder in Fig. 16. The integrated pressure on the front, i.e., $-45° < \phi < 45°$ is considerably larger than that on the back side at the moment of main peak ($t = 13.14$ s). With further development of flow, the integrated pressure on the front side decreases, while on the back side it increases. Therefore, the net inline force reduces after the main peak.

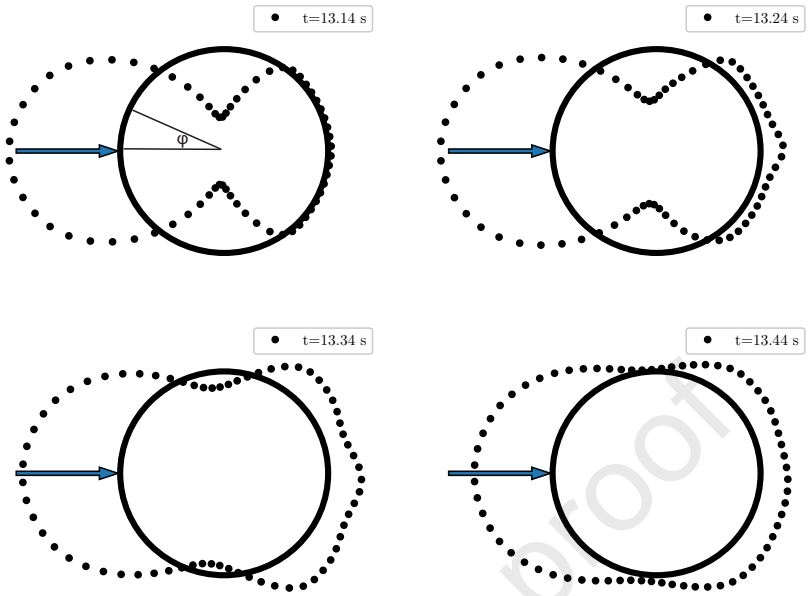

Figure 16: Distribution of the total pressure integration in the circumference direction from $\phi = 0°$ to $\phi = 360°$, where $\phi = 0°$ corresponds to the front stagnation of the cylinder. The pressure is integrated from the bottom to the instantaneous free surface. The dots outside the cylinder represent positive pressure integration i.e., acting into the cylinder, and vice versa. The results are from the surging-breaker case. The incident wave condition is $H = 0.20$ m, $R_c = 0.15$ m and $T = 3$ s.

In Chen et al. (2015), the inline force is scaled with the maximum momentum flux $(U^2d)_m$. This is also confirmed in Fig. 17, which shows the time series of the momentum flux carried by the overtopping flow and the inline force. For the surging-breaker case, the development of the momentum flux perfectly matches the inline force, indicating a close correlation. The slight discrepancy after the main peak is due to the wake effect, which will be explained in Section 5.3. Regarding the plunging-breaker case, certain oscillations are observed for the momentum flux due to entrained air in the overtopping flow. It induces oscillations on the overtopping flow depth d, as explained in Section 2.3, which further results in the oscillation of U^2d. However, the main peak of the overtopping flow is still aligned with the maximum momentum flux, as in the surging-breaker case.

From the experimental results in Part I, the decay of the main peak with the distance x to the edge of the seawall can be described by an exponential function

$$\frac{F_m(x)}{F_{0m}} = \exp\left[-0.059\left(\frac{x_c - x_{c0}}{d_{0m}}\right)^{0.66}\right], \qquad 0 < \frac{x_c - x_{c0}}{d_{0m}} < 45, \tag{11}$$

where $F_m(x)$ is the main peak at location x, and F_{0m} is the main peak at the edge of the seawall crest (see Part I for more details). x_c is the location of the cylinder centre and x_{c0} is $1.5D$. If the main peak is indeed well scaled with the momentum flux, Eq. (11) should also be applicable to describe the $x-$decay of the

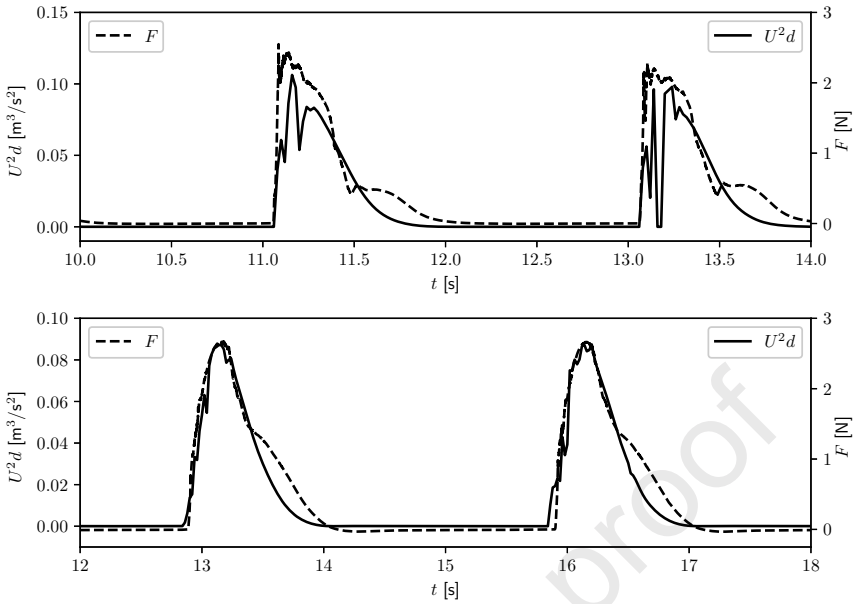

Figure 17: Time series of the momentum flux U^2d carried by the overtopping flow and the inline force on the cylinder F at the edge of the seawall for the plunging-breaker case (upper) and surging-breaker case (lower).

maximum momentum flux. This has been confirmed in Fig. 18, which presents the decay of the maximum momentum flux along the seawall crest. The data in Fig. 18 are from the same 2D simulations as shown in Section 3. It is observed that in Fig. 18, the decay of the maximum momentum flux is reasonably described by the same exponential decay function with ±30% uncertainty, which is the same uncertainty range for the x-decay of the inline force. This shows that the main peak of the inline force is indeed correlated with the maximum momentum flux.

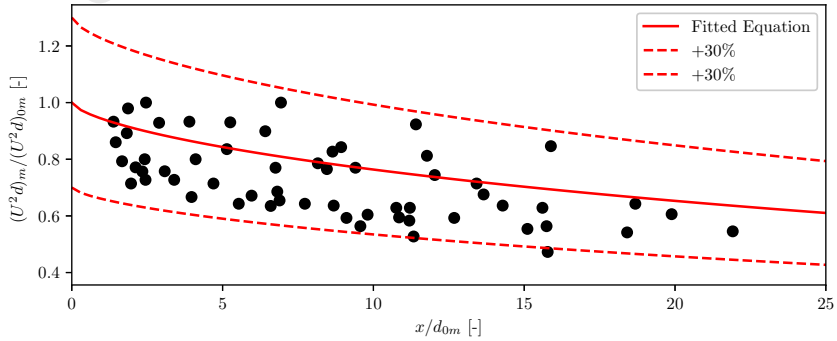

Figure 18: Decay of the maximum momentum flux $(U^2d)_m$ along the seawall crest. The fitted equation is Eq. (17), which is based on the inline force measured from the experiments.

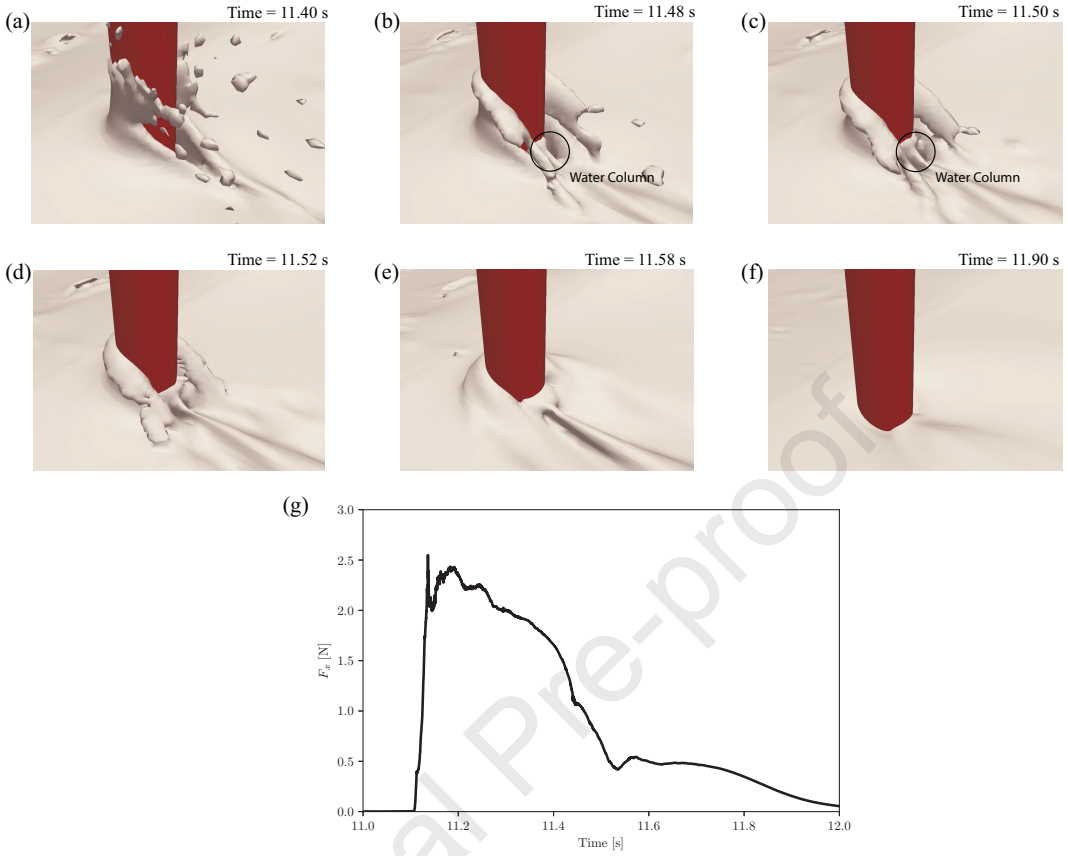

Figure 19: (a-f) Snapshots of the free surface near the cylinder around the time when secondary load cycle occurs: (a) at the time of the overtopping flow passing the front side of the cylinder, (b) at the time when the water column starts to build, (c) at the time during the water column grows, (d) at the time when the water column reaches its maximum and starts to fall down, (e) at the time when the water column is collapsing, (f) at the end of the secondary load cycle. The results are from the plunging-breaker case. The incident wave condition is $H = 0.20$ m, $R_c = 0.15$ m and $T = 2$ s. (g) The corresponding time series of the inline force on the cylinder.

5.3. Secondary load cycle

A secondary load cycle, which appears after the main peak (as illustrated in Fig. 13), is often observed for the plunging breaker cases. This feature of the inline force is strongly related to the local flow in the back side of the cylinder. Fig. 19 presents a few snapshots for the flow near the cylinder during the secondary load cycle for the plunging-breaker case. In Fig. 19(a) when the overtopping flow just passes the front side of the cylinder, the flow appears to be separated from the back of the cylinder, and a dry zone is formed behind the cylinder. Then the water quickly flows into the dry zone, and a small water column starts to build in the wake, as indicated by the circle in Fig. 19(b). The water column continues to grow in Fig. 19(c), which reaches its maximum in Fig. 19(d) and begins to fall down. Fig. 19(e) shows the collapsing of the water column, which lasts until the end of the second load cycle in Fig. 19(f).

As mentioned above, the water column is built due to the returned flow into the dry zone. This actually creates a positive pressure zone (pointing towards the cylinder) that partially counterbalances the inline force. The secondary load cycle is found to be associated with the fall-down process of the water column in the back. The 'dip' of the inline force, which marks the beginning of the secondary load cycle, occurs at $t = 11.52$ s when the water column reaches its maximum. With the decreasing of the water column height, the pressure in the wake zone is further reduced, and this decay is faster than the decay of pressure force acting on the front side of the cylinder. This gives rise to an increased inline force, which appears to be a secondary cycle in the time series of the inline force.

Similar findings on the secondary load cycle have been documented in previous publications (Ghadirian and Bredmose, 2020; Paulsen et al., 2014; Riise et al., 2018) mainly in the context of wave-cylinder interaction. There is a strong analogy between these two contexts, as the secondary load cycle in both cases are related to the nonlinear free surface deformation behind the cylinder. In our case, there is a clear dry zone that is filled by the returned flow towards the back side of the cylinder. This explains why the secondary load cycle only occurs under steep plunging wave overtopping, as the local Froude number is high enough to provide a strong flow with high speed. This is the prerequisite for the flow separation and the dry zone to occur.

6. Predictor of maximum inline force

6.1. Calibration

In Part I, a predictor has been developed for quick estimation of the maximum inline force F_{0m} (the main peak) acting on the human standing at the edge of the seawall crest. Here F_{0m} is scaled with square of wave height. The scaling parameter C_H is determined by the relative freeboard R_c/H and I_r, and F_{0m} is calculated as

$$F_{0m} = C_H \left(I_r, \frac{R_c}{H} \right) \cot\beta \, \rho g H^2 D \tag{12}$$

where ρ, g are the density of water and gravitation, β is the slope of the seawall, D is the equivalent diameter, which is demonstrated to be about 1.4 times the width of a human thigh as shown in Part I. In Section 5.2, we have shown that F_{0m} is correlated with the maximum momentum flux $(U^2 d)_{0m}$ at seawall's leading edge. Note that the both U^2 and d are scaled with $R_u - R_c$ (see e.g., EurOtop (2018); Schüttrumpf and Oumeraci (2005)), where R_u is the overtopping run-up on an infinite-long slope, which can be estimated as $R_u = I_r H$ (Schüttrumpf and Oumeraci, 2005). Thus, $(U^2 d)_{0m}$ is scaled with $(I_r - R_c/H)^2 H^2$. In Eq. (12), the influence of $I_r - R_c/H$ is absorbed in the parameter C_H, so this H-scaling, although appears oversimplified, is likely to be equivalent to a $U^2 d$-scaling. Fig. 20 presents C_H as a function of the non-dimensional momentum flux $(U^2 d)_{0m}/gH^2$, where the test conditions for the data points are given in Table

Table 4: Test conditions for the data points in Fig. 20.

h [m]	R_c [m]	H [m]	T [s]	Slope [-]
0.92	0.08	0.16	3	1:3
0.84	0.16	0.16	3	1:3
0.85	0.15	0.15	3	1:3
0.76	0.24	0.16	3	1:3

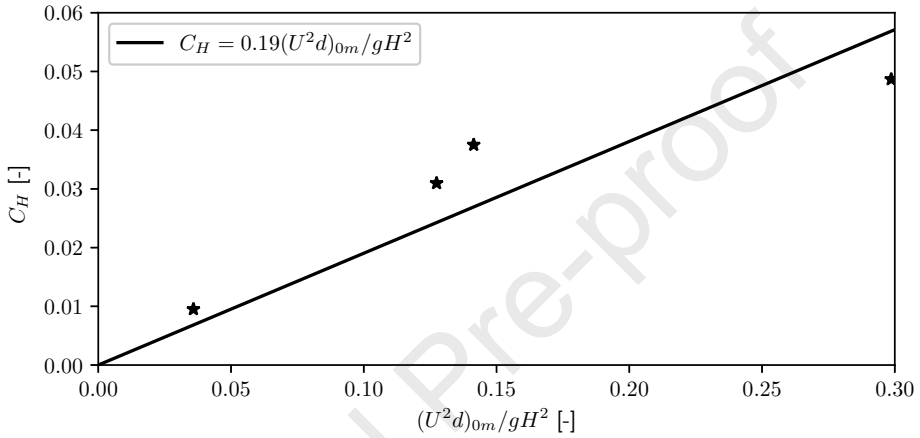

Figure 20: Correlation between the nondimensional momentum flux $(U^2d)_{0m}/(gH^2)$ and the scaling parameter C_H.

4. From Fig. 20, it seems that a linear relation can be established between C_H and $(U^2d)_{0m}/gH^2$, i.e.

$$C_H = \frac{C}{gH^2}(U^2d)_{0m} \tag{13}$$

where $C = 0.19$. A U^2d scaling law can be obtained by substituting Eq. (13) into Eq. (12)

$$F_{0m} = C \cot\beta \rho D (U^2d)_{0m} \tag{14}$$

Apparently, this scaling law and the scaling parameter C need more data to support, but the rest of our simulations unfortunately only output the time series of inline force due to limited storage. Also, it is very difficult to get direct prediction of the momentum flux unless one uses a process-based numerical model. Thus, in the present manuscript, we primarily focus on the $H-$scaling, i.e. Eq. (12), for its simplicity.

The scaling parameter C_H is calibrated based on a large dataset that includes test conditions covering various values of I_r, R_c/H and β. The experimental dataset only has a 1:3 slope, and all tests are in model-scale. To expand the dataset, additional 65 numerical simulations were conducted for the slope of 1:2, 1:3 and 1:4 at prototype-scale. The test conditions are summarised in Table 5. The mesh used in the model-scale described in Section 2 is directly scaled-up to be used for the simulations at prototype-scale. It is expected that this resolution should be sufficient to capture the main peak, which is essentially dominated by inertia

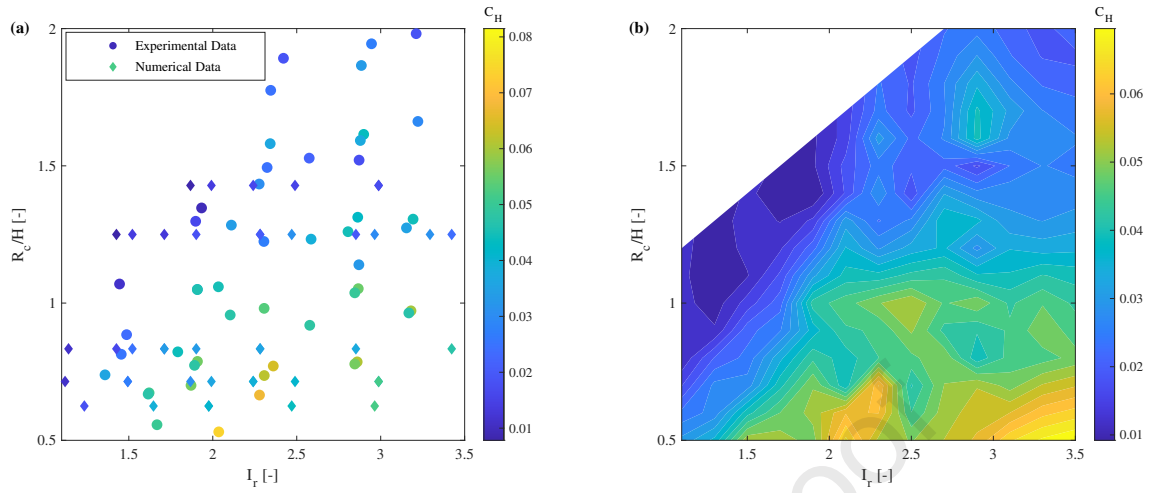

Figure 21: (a) The numerically and experimentally derived data points for C_H. (b) The contour of C_H as a function of I_r and R_c/H.

Table 5: Test conditions in the numerical simulations at prototype-scale.

h [m]	R_c [m]	H [m]	T [s]	I_r [-]
$2.5 \sim 3.5$	$0.5 \sim 1.5$	$0.4 \sim 1.6$	$3 \sim 6$	$1.1 \sim 3.5$

effects as shown in Section 5.2. The experimentally and numerically derived C_H are presented in Fig. 21(a), respectively. Both the numerically and experimentally derived C_H have the same trend of variation, i.e., C_H decreases with the increasing R_c/H and decreasing I_r. An 10% - 20% underestimate by the numerical model is observed, which is consistent with the observation in Section 3. In Fig. 21(b), these data points are linearly interpolated onto a uniform $R_c/H - I_r$ grid, covering R_c/H within $(0.5, 2)$ and I_r within $(0.5, 3.5)$. The white upper left corner indicates the conditions that wave overtopping is extremely weak or prevented by a large freeboard. The interpolated $C_H = f(R_c/H, I_r)$ is provided in the supplementary materials.

We evaluate the accuracy of the calibrated Eq. (12) to the cases in the experimental and numerical dataset, respectively in Fig. 22(a) and Fig. 22(b). Generally speaking, the predictor works equally well for both numerical and experimental datasets. The model inaccuracy is mostly less than 30%. The main peak in the scaled lab tests is underpredicted by about 12% (i.e., in Fig. 22(a) the best fit to the data cloud is $F_p = 0.88F_m$, where F_p is given by the predictor and F_m is the measurements), while the main peak in the prototype numerical simulations is overestimated by about 5% (i.e., in Fig. 22(b) the best fit is $F_p = 1.05F_s$, where F_s is the simulated force). This is in agreement with model validation shown in Section 3, where our numerical model underestimates the main peak by $10 - 20\%$. Since the predictor is calibrated based on the combined dataset, it should give some overestimates for the numerical cases but some underestimates for

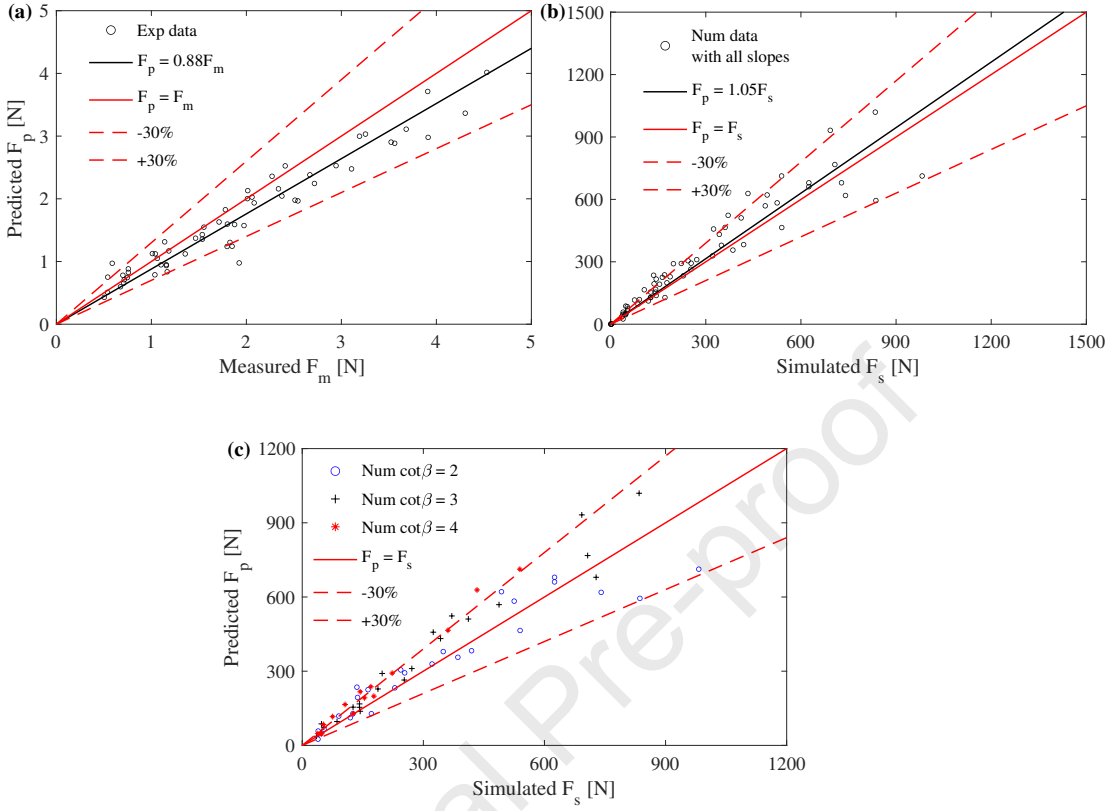

Figure 22: (a) Comparison of the measured force in the experiments and the predicted force using the H-scaling predictor, i.e. Eq. (12). These experiment-only data points fit into a line of $F_p = 0.88F_m$. (b) Comparison of the simulated force from the numerical model and the predicted force using the H-scaling formula, i.e. Eq. (12). These simulation-only data points fit into a line of $F_p = 1.05F_s$. (c) The simulated force with slopes of 1:2, 1:3 and 1:4.

the experimental cases.

The validation for the numerical cases is further broken down into three groups with three seawall slopes (1:2, 1:3 and 1:4) in Fig. 22(c). The best fits for the three data clouds are $F_p = 0.91F_s$ (1:2 slope), $F_p = 1.18F_s$ (1:3 slope), and $F_p = 1.36F_s$ (1:4 slope). This means that there is a model bias induced by seawall slope. The predictor overestimates the main peak for 1:4, but this overestimate is reduced as the slope is reduced to 1:3. For 1:2 slope, when the resultant force on the cylinder is relatively small ($< 300\,\mathrm{N}$), the predictor produces a slight overestimate. With the increase of the force, the overestimate is reduced and eventually for some large forces ($> 700\,\mathrm{N}$), we found an underestimate by the predictor, which may give unconservative results for risk assessment. The model bias is likely due to the assumption introduced in the predictor. In Eq. (12), the main influence of slope angle is captured by $\cot\beta$. This assumption is borrowed from Chen et al. (2015), who proposed a similar predictor for maximum overtopping force on a vertical

wall. They introduced this $\cot\beta$ based on fitting their measurements, so it can be argued that the $\cot\beta$ term in Eq. (12) is empirical, and may not be very accurate. Nevertheless, this assumption significantly reduces the required number of experimental and numerical data points, as C_H is assumed to be a function of only two variables instead of three. Considering that the approximation of human body as an cylinder will inevitably introduce some uncertainties that is comparable to 30%, we consider this calibration of C_H and the predictor are accurate enough for engineering application, but the model's applicability must be limited to slope ranges from 1:4 to 1:2.

6.2. Application of the predictor for field irregular waves

The predictor introduced in Section 6.1 is for regular wave, while field waves are always irregular. One way to deal with the irregularity is the so-called wave-by-wave approach. Namely, we treat a train of irregular waves as an ensemble of individual regular waves, so the force predictor can be applied wave-by-wave to quickly estimate the maximum inline force under each wave cycle. Coastal waves are often assumed to have a narrow spectrum, and the spreading of wave traveling direction is limited by wave refraction, so such a wave-by-wave approximation may work well. To test this idea, numerical simulations were conducted, in which irregular waves are normally incident towards a sloped seawall. The mesh is the same as the one used for obtaining additional prototype-scale data in Section 6.1, and the slope used here is 1:3. Using the high-fidelity numerical model, the inline force of a cylinder on the seawall's edge can be directly simulated, and the results are to be compared with those given by wave-by-wave applying the simple force predictor. The incident waves are divided into individual waves by applying a zero-crossing analysis to the recorded surface elevation at the offshore boundary. Therefore, for each individual i-th wave cycle, the wave height H_i and wave period T_i can be determined, which is further used to obtain F_{0m} for each cycle.

Two sets of irregular wave tests were conducted in parallel, in order to obtain more data points. JONSWAP spectrum was used in both cases with significant wave height $H_s = 0.8$ m and 1 m, respectively. In both cases, the peak period $T_p = 6$ s, the enhancement factor $\gamma = 3.3$ and the freeboard $R_c = H_s$. For each test, a duration of 160 s (about 30 waves) simulation could be completed with 24 cores within 2 weeks. Fig. 23 shows the time series of surface elevation near the wave inlet and the inline force due to overtopping flow for the case with $H_s = 0.8$ m. The effect of wave irregularity on overtopping is primarily on the breaking process. The run-down of overtopping flow on the seawall slope will interfere the breaking of the next wave, so a wave in an irregular wave train may not break in the same way when it is in a regular wave train. This effect, however, is found to be insignificant for the prediction of the maximum inline force. As shown in Fig. 17, the relative difference between the directly simulated (F_s) maximum inline force and the estimate (F_p) using the empirical predictor is generally within 30%, which is in agreement of the accuracy of the predictor shown in the right figure of Fig. 23. This suggests that the force predictor can indeed be used in real applications via a wave-by-wave approach.

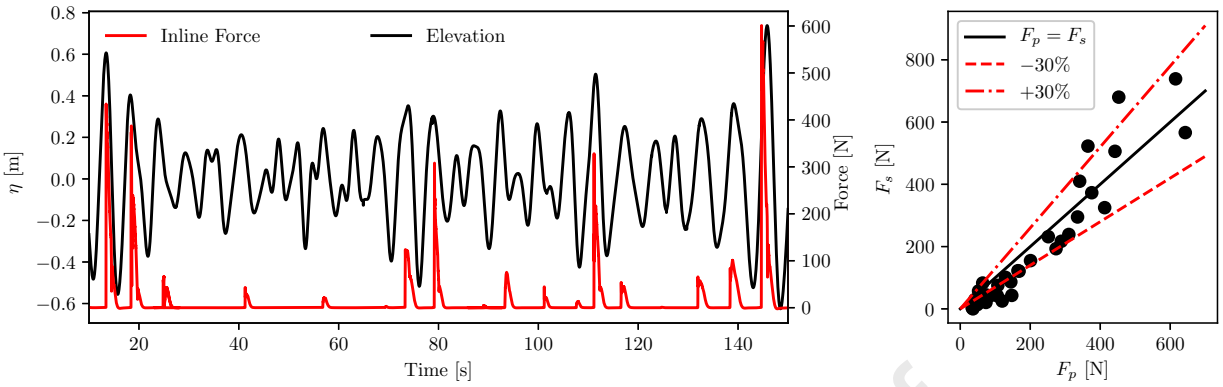

Figure 23: Left: Comparison of the time series of the surface elevation near the inlet of the wave tank and the induced inline force on the cylinder due to the overtopping flow under irregular wave conditions. The time series have been aligned to enable a wave-to-wave analysis. The incident irregular wave condition is based on the JONSWAP spectrum with a significant wave height H_s of 0.8 m, peak period T_p of 6 s and freeboard R_c of 1 m. Right: Comparison between the predicted force F_p using the derived formula in Eq. (12) and the simulated force F_s from both cases with irregular wave conditions.

7. Summary and conclusions

The interaction of overtopping flow with a cylinder as a surrogate of human body is numerically investigated in the present paper, where a VOF based RANS model with $k-\omega$ SST turbulence closure model is utilised. With a reasonable resolution of about 3 million cells, the model can properly resolve wave propagation, breaking on the slope, overtopping and the 3-dimensional interaction between the overtopping flow and the cylinder. The numerical model is validated against experimental data obtained from Part I, which shows that the model is capable to capture the general shape and the peaks of the overtopping flow depth and the inline force.

The characteristics of overtopping flow velocity is investigated based on a variety of 2D numerical simulations. It is found that the maximum overtopping flow velocity occurs before the maximum depth-averaged flow velocity in an overtopping event. With the development of the overtopping flow, the velocity profile tends to become uniformly distributed across the depth. The Froude number of the overtopping flow at the edge of the seawall decreases linearly with the increase of the Iribarren number. Decay of the overtopping flow velocity is not obvious, as most of the data fall within the range of $0.7 < U_m(x)/U_{0m} < 1.2$ for a distance of $x/d_{0m} < 30$.

Regarding the inline force on the cylinder, it is observed that for the surging-breaker case, the inline force is dominated by the main peak. However, time series of the inline force for the plunging-breaker case suggests that during one overtopping event, there can be a first impact, a main and a secondary peaks. The first impact peak is generated when the tip of the overtopping flow slams onto the cylinder, and is strongly associated with the local flow at the tip. There is a strong cycle-to-cycle variation as the tip flow is not

exactly repetitive. Meanwhile, the main peak is dominated by the inertia effects. By extracting the pressure distribution around the cylinder, it is found that the main peak is driven by the asymmetric distribution in the front and back side of the cylinder. The time series of inline force curve is aligned well with the momentum flux of the overtopping flow, indicating they are highly correlated. The secondary load cycle is associated with the complex flow behind the cylinder. A water column at the back side of the column is built due to the returned flow, and the secondary peak is produced by the collapsing of this water column.

The validated numerical wave flume was used to generate overtopping flows that could not be obtained in the experiments in Part I. Namely, a large sets of simulations for seawalls with different slopes (1:2, 1:3 and 1:4) at prototype scale were conducted to collect data of the maximum inline force (the main peak) on the cylinder. By combining physical and numerical simulations, a large dataset was developed for calibrating a simple predictor for the maximum inline force. Finally, a numerical experiment involving irregular incident waves was conducted to demonstrate that the simple predictor can be used for real application in a wave-by-wave approach.

The two companion papers combine experimental and numerical modelling to investigate the wave overtopping on a sloped seawall and its interaction with a cylinder. The experiments provide direct observations of the overall physical process, as well as the measurements of some key physical quantities (e.g., the inline force). The validated numerical model provides comprehensive information on the overtopping flow velocity and the pressure distribution around the cylinder, which cannot be measured in the experiments. Moreover, the numerical model was applied to expand the dataset for calibrating empirical formula. In recent years, high-fidelity numerical modelling is becoming tangible because of the fast advancement of supercomputing resources and open-source codes. We believe that numerical modelling will have more weightage in the future coastal-engineering research, and such a combined numerical and experimental research will become more popular. This study is limited to wave overtopping at a sloped (and impermeable) seawall with a deep foreshore, which is motivated by the revetments protecting the reclaimed land in Singapore. This is only a small piece of the entire overtopping framework, so future work is needed to cover more topographic and flow conditions, e.g., seawalls with a shallow foreshore, porous structure, seawalls with berms, obliquely incident waves etc.

Acknowledgement

This work was supported by the Climate Resilience Study Funds (CRSF) through Building and Construction Authority (BCA) and Public Utilities Board (PUB) of Singapore. The Department of Civil and Environmental Engineering in National University of Singapore is acknowledged for allowing us to use the hydraulic laboratory. National Supercomputing Centre Singapore (NSCC) is acknowledged for providing the high-performance computing facilities for the present study.

Allsop W, Bruce T, Pearson J, Alderson J, Pullen T. Violent wave overtopping at the coast, when are we safe? In: International Conference on Coastal Management 2003. Thomas Telford Publishing; 2003. p. 54–69.

Altomare C, Suzuki T, Chen X, Verwaest T, Kortenhaus A. Wave overtopping of sea dikes with very shallow foreshores. Coastal Engineering 2016;116:236–57. doi:10.1016/j.coastaleng.2016.07.002.

Bakhtyar R, Barry DA, Yeganeh-Bakhtiary A, Ghaheri A. Numerical simulation of surf–swash zone motions and turbulent flow. Advances in Water Resources 2009;32(2):250–63.

Bosman G, Van Der Meer J, Hoffmans G, Schüttrumpf H, Verhagen HJ. Individual overtopping events at dikes. In: Coastal Engineering 2008: (In 5 Volumes). World Scientific; 2009. p. 2944–56.

Bradford SF. Numerical simulation of surf zone dynamics. Journal of Waterway, Port, Coastal, and Ocean Engineering 2000;126(1):1–13.

Cao D, Yuan J, Chen H, Zhao K, Liu PLF. Wave overtopping flow striking a cylinder on the crest of a sloped seawall. part i: An experimental study; 2021. Unpublished.

Chella MA, Bihs H, Myrhaug D, Muskulus M. Hydrodynamic characteristics and geometric properties of plunging and spilling breakers over impermeable slopes. Ocean Modelling 2016;103:53–72.

Chen X, Hofland B, Altomare C, Suzuki T, Uijttewaal W. Forces on a vertical wall on a dike crest due to overtopping flow. Coastal Engineering 2015;95:94–104. doi:10.1016/j.coastaleng.2014.10.002.

Chen X, Hofland B, Uijttewaal W. Maximum overtopping forces on a dike-mounted wall with a shallow foreshore. Coastal Engineering 2016;116:89–102. URL: http://dx.doi.org/10.1016/j.coastaleng.2016.06.004. doi:10.1016/j.coastaleng.2016.06.004.

Chuang WL, Chang KA, Mercier R. Green water velocity due to breaking wave impingement on a tension leg platform. Experiments in Fluids 2015;56(7):139.

Chuang WL, Chang KA, Mercier R. Kinematics and dynamics of green water on a fixed platform in a large wave basin in focusing wave and random wave conditions. Experiments in Fluids 2018;59(6):100.

De Finis S, Romano A, Bellotti G. Numerical and laboratory analysis of post-overtopping wave impacts on a storm wall for a dike-promenade structure. Coastal Engineering 2020;155:103598.

De Rouck J, Van Doorslaer K, Versluys T, Ramachandran K, Schimmels S, Kudella M, Trouw K. Full scale impact tests of an overtopping bore on a vertical wall in the large wave flume (gwk) in hannover. Coastal Engineering Proceedings 2012;1(33):structures–62.

EurOtop . Manual on wave overtopping of sea defences and related structures. an overtopping manual largely based on european research, but for worldwide application. Van der Meer, J W and Allsop, N W H and Bruce, T and De Rouck, J and Kortenhaus, A and Pullen, T and Schüttrumpf, H and Troch, P and Zanuttigh, B 2018;.

Ghadirian A, Bredmose H. Detailed force modelling of the secondary load cycle. Journal of Fluid Mechanics 2020;889:A21. URL: https://www.cambridge.org/core/product/identifier/S0022112020000701/type/journal{_}article. doi:10.1017/jfm.2020.70.

Hirt CW, Nichols BD. Volume of fluid (vof) method for the dynamics of free boundaries. Journal of computational physics 1981;39(1):201–25.

Hsiao SC, Lin TC. Tsunami-like solitary waves impinging and overtopping an impermeable seawall: Experiment and rans modeling. Coastal Engineering 2010;57(1):1–18.

Hu K, Mingham CG, Causon DM. Numerical simulation of wave overtopping of coastal structures using the non-linear shallow water equations. Coastal engineering 2000;41(4):433–65.

Hughes SA. Estimation of wave run-up on smooth, impermeable slopes using the wave momentum flux parameter. Coastal Engineering 2004a;51(11):1085 –104. URL: http://www.sciencedirect.com/science/article/pii/S0378383904000985. doi:https://doi.org/10.1016/j.coastaleng.2004.07.026.

Hughes SA. Wave momentum flux parameter: a descriptor for nearshore waves. Coastal Engineering 2004b;51(11):1067–84. URL: http://www.sciencedirect.com/science/article/pii/S0378383904000924. doi:https://doi.org/10.1016/j.coastaleng.2004.07.025.

Jacobsen NG, Fuhrman DR, Fredsøe J. A wave generation toolbox for the open-source CFD library: OpenFoam®. International Journal for Numerical Methods in Fluids 2012;70(9):1073–88. doi:10.1002/fld.2726.

Jonkman S, Penning-Rowsell E. Human instability in flood flows 1. JAWRA Journal of the American Water Resources Association 2008;44(5):1208–18.

Kihara N, Niida Y, Takabatake D, Kaida H, Shibayama A, Miyagawa Y. Large-scale experiments on tsunami-induced pressure on a vertical tide wall. Coastal engineering 2015;99:46–63.

Lin P, Liu PLF. A numerical study of breaking waves in the surf zone. Journal of fluid mechanics 1998;359:239–64.

Losada IJ, Lara JL, Guanche R, Gonzalez-Ondina JM. Numerical analysis of wave overtopping of rubble mound breakwaters. Coastal engineering 2008;55(1):47–62.

Mares-Nasarre P, Argente G, Gómez-Martín ME, Medina JR. Overtopping layer thickness and overtopping flow velocity on mound breakwaters. Coastal Engineering 2019;154(September). doi:10.1016/j.coastaleng.2019.103561.

Martínez-Gomariz E, Gómez M, Russo B. Experimental study of the stability of pedestrians exposed to urban pluvial flooding. Natural hazards 2016;82(2):1259–78.

Van der Meer J, Bruce T. New Physical Insights and Design Formulas on Wave Overtopping at Sloping and Vertical Structures. Journal of Waterway, Port, Coastal, and Ocean Engineering 2013;140(6):04014025. doi:10.1061/(asce)ww.1943-5460.0000221.

Van der Meer JW, Verhaeghe H, Steendam GJ. The new wave overtopping database for coastal structures. Coastal Engineering 2009;56(2):108–20. URL: http://dx.doi.org/10.1016/j.coastaleng.2008.03.012. doi:10.1016/j.coastaleng.2008.03.012.

Molines J, Herrera MP, Gómez-Martín ME, Medina JR. Distribution of individual wave overtopping volumes on mound breakwaters. Coastal Engineering 2019;149(December 2018):15–27. URL: https://doi.org/10.1016/j.coastaleng.2019.03.006. doi:10.1016/j.coastaleng.2019.03.006.

Paulsen BT, Bredmose H, Bingham HB, Jacobsen NG. Forcing of a bottom-mounted circular cylinder by steep regular water waves at finite depth. Journal of Fluid Mechanics 2014;755:1–34. doi:10.1017/jfm.2014.386.

Pullen T, Allsop W, Bruce T, Pearson J. Field and laboratory measurements of mean overtopping discharges and spatial distributions at vertical seawalls. Coastal Engineering 2009;56(2):121–40. URL: http://dx.doi.org/10.1016/j.coastaleng.2008.03.011. doi:10.1016/j.coastaleng.2008.03.011.

Riise BH, Grue J, Jensen A, Johannessen TB. A note on the secondary load cycle for a monopile in irregular deep water waves. Journal of Fluid Mechanics 2018;849.

Roenby J, Bredmose H, Jasak H. A computational method for sharp interface advection. Royal Society Open Science 2016;3(11). doi:10.1098/rsos.160405.

Romano A, Bellotti G, Briganti R, Franco L. Uncertainties in the physical modelling of the wave overtopping over a rubble mound breakwater: The role of the seeding number and of the test duration. Coastal Engineering 2015;103:15–21. URL: http://dx.doi.org/10.1016/j.coastaleng.2015.05.005. doi:10.1016/j.coastaleng.2015.05.005.

Russo B, Gómez M, Macchione F. Pedestrian hazard criteria for flooded urban areas. Natural hazards 2013;69(1):251–65.

Ryu Y, Chang KA. Green water void fraction due to breaking wave impinging and overtopping. Experiments in Fluids 2008;45(5):883–98. doi:10.1007/s00348-008-0507-3.

Ryu Y, Chang KA, Mercier R. Runup and green water velocities due to breaking wave impinging and overtopping. Experiments in Fluids 2007;43(4):555–67. doi:10.1007/s00348-007-0332-0.

Schüttrumpf H, Oumeraci H. Layer thicknesses and velocities of wave overtopping flow at seadikes. Coastal Engineering

2005;52(6):473–95. doi:10.1016/j.coastaleng.2005.02.002.

Shafiei S, Melville BW, Shamseldin AY. Experimental investigation of tsunami bore impact force and pressure on a square prism. Coastal Engineering 2016;110:1–16. doi:10.1016/j.coastaleng.2015.12.006.

Stansby PK, Feng T. Surf zone wave overtopping a trapezoidal structure: 1-d modelling and piv comparison. Coastal Engineering 2004;51(5-6):483–500.

Van Bergeijk V, Warmink J, van Gent M, Hulscher S. An analytical model of wave overtopping flow velocities on dike crests and landward slopes. Coastal Engineering 2019;149(March):28–38. doi:10.1016/j.coastaleng.2019.03.001.

Van Doorslaer K, Romano A, De Rouck J, Kortenhaus A. Impacts on a storm wall caused by non-breaking waves overtopping a smooth dike slope. Coastal Engineering 2017;120(December 2016):93–111. URL: http://dx.doi.org/10.1016/j.coastaleng.2016.11.010. doi:10.1016/j.coastaleng.2016.11.010.

Wang Z, Zou Q, Reeve D. Simulation of spilling breaking waves using a two phase flow cfd model. Computers & Fluids 2009;38(10):1995–2005.

Xie Z. Two-phase flow modelling of spilling and plunging breaking waves. Applied Mathematical Modelling 2013;37(6):3698–713. URL: http://dx.doi.org/10.1016/j.apm.2012.07.057. doi:10.1016/j.apm.2012.07.057.

Yeh H. Maximum Fluid Forces in the Tsunami Runup Zone. Journal of Waterway, Port, Coastal, and Ocean Engineering 2006;132(6):496–500. URL: http://www.worldscientific.com/doi/abs/10.1142/9789812774613{_}0018http://ascelibrary.org/doi/10.1061/{%}28ASCE{%}290733-950X{%}282006{%}29132{%}3A6{%}28496{%}29. doi:10.1061/(ASCE)0733-950X(2006)132:6(496).

Highlight

1. The inline force on a cylinder as a surrogate of human body due to wave overtopping flow is thoroughly investigated by a 3-dimensional VOF based RANS model.

2. The numerical model is carefully validated against the experimental data for both plunging-breaker and surging breaker cases.

3. The inline force generated by a plunging-breaker induced overtopping flow usually comprises a cycle of a first impact peak, a main peak and a secondary peak, while the inline force due to surging-breaker induced overtopping flow is dominated by the main peak.

4. Numerical experiments are performed on irregular wave overtopping a sloped seawall, which demonstrates the applicability of the force predictor developed in Part I.

Declaration of interests

☒ The authors declare that they have no known competing financial interests or personal relationships that could have appeared to influence the work reported in this paper.

☐The authors declare the following financial interests/personal relationships which may be considered as potential competing interests: